Regenerative Therapy 21 (2022) 122–138

Contents lists available at ScienceDirect

Regenerative Therapy

journal homepage: http://www.elsevier.com/locate/reth

Original Article

Fabrication of Biologically Inspired Electrospun Collagen/Silk fibroin/bioactive glass composited nanofibrous scaffold to accelerate the treatment efficiency of bone repair

Jianjun Wu [a, b, *], Shengxuan Wang [a, b], Zhong Zheng [a, b], Jianbao Li [a, b]

[a] Department of Spine Surgery, The Third Clinical Medical College, Fujian Medical University
[b] Department of Spine Surgery, Fuzhou Second Hospital, PR China

ARTICLE INFO

Article history:
Received 28 November 2021
Received in revised form
15 April 2022
Accepted 15 May 2022

Keywords:
Collagen
Silk fibroin
Bioactive glass nanoparticles
Composite nanofiber
Osteoporotic bone defect

ABSTRACT

Bone disease and disorder treatment might be difficult because of its complicated nature. Millions of patients each year need bone substitutes that may help them recover quickly from a variety of illnesses. Synthetic bone replacements that mirror the structural, chemical, and biological features of bone matrix structure will be very helpful and in high demand. In this research, the inorganic bioactive glass nanoparticles matrixed with organic collagen and silk fibroin structure (COL/SF/CaO-SiO_2) were used to create multifunctional bone-like fibers in this study, which we describe here. The fiber structure is organized in a layered fashion comparable to the sequence in which apatite and neo tissue are formed. The amino groups in COL and SF combined with CaO-SiO_2 to stabilize the resulting composite nanofiber. Morphological and functional studies confirmed that crystalline CaO-SiO_2 nanoparticles with average sizes of 20 ± 5 nm are anchored on a 115 ± 10 nm COL/SF nanofiber matrix. X-ray photoelectron spectroscopic (XPS) results confirmed the presence of C, N, O, Ca, and Si in the composite fiber with an atomic percentage of 59.46, 3.30, 20.25, 3.38 and 13.61%. respectively. The biocompatibility examination with osteoblast cells (Saos-2) revealed that the CAL/SF/CaO-SiO_2 composite nanofiber had enhanced osteogenic activity. Finally, when the CAL/SF/CaO-SiO_2 composite nanofiber scaffolds were used to treat an osteoporotic bone defect in a rat model, the composite nanofiber scaffolds significantly promoted bone regeneration and vascularization. This novel fibrous scaffold class represents a potential breakthrough in the design of advanced materials for complicated bone regeneration.

1. Introduction

Osteoporosis is a common metabolic bone condition that affects more than 200 million people worldwide each year [1]. In this situation, the balance between bone regeneration and mineralization is disrupted. As a result, osteoporotic patients' bone density, strength, and microarchitectures are considerably reduced, increasing their risk of fracture, sickness, and even death [2]. In this circumstance, preventing further fractures by promoting bone regeneration is crucial for osteoporosis treatment [3]. Nowadays, a variety of techniques have been developed to stimulate bone regeneration in the context of osteoporosis therapy. Conventional pharmacological therapy, including anti-resorptive and anabolic medications, has proven ineffectual owing to the low absorption and toxicity of these drugs [4]. On the other hand, different endosseous implants and bridging materials have been demonstrated to be ineffectual in terms of achieving a suitable therapeutic effect [5]. As a consequence, the development of an effective treatment approach for stimulating bone regeneration in a complicated pathological environment is crucial.

Recently, bioactive glasses (BAGs) have garnered considerable interest because of their potential applications in biological fields such as tissue engineering [6], drug delivery [7], wound healing, etc. BAGs (mainly CaO-SiO_2) exhibited excellent osteoconductive and osteoinductive properties, facilitating bone formation via chemical interactions with the surrounding bone tissue [8].

* Corresponding author. No. 47, Shangteng Road, Cangshan District, Fuzhou 350007, Fujian Province, China.
E-mail address: wujianjun86@yahoo.com (J. Wu).
Peer review under responsibility of the Japanese Society for Regenerative Medicine.

https://doi.org/10.1016/j.reth.2022.05.006

Additionally, the breakdown products of BAG ions, such as Ca^{2+} and Si^{2+}, result in the creation of a hydroxyapatite-like layer, modify osteogenic gene expression, and promote angiogenesis, all of which are necessary for bone tissue regeneration [9]. Additionally, in vivo tests indicated that BAGs boosted osteoblast proliferation and differentiation and promoted new bone formation [10]. In clinics, bone void fillers or bone grafts composed of biomaterials containing BAGs are currently being used to enhance bone repair. However, the intrinsic stiffness and brittleness of BAGs limit their use as scaffolds for bone tissue engineering [11]. Polymers with the desired flexibility and mechanical strength were then combined with BAG nanoparticles (BAGNPs) to create a composite flexible scaffold [12]. Indeed, the nano-sized formulation facilitated the development of extracellular matrix rather than impairing BAGs bioactivity [13]. Additionally, the hybrid composites of inorganic BAGNPs and organic polymers mimic the natural structure of the bone matrix, which is composed of organic collagenous (COL) silk fibroin (SF) fibers embedded in CaO-SiO_2 nanocrystallites [14].

In this research collagen (COL) and silk fibroin (SF) molecules derived from silkworm (*Bombyx mori*) cocoons were used as an organic component to combine with MABGNPs. As the most abundant, biodegradable, and biocompatible protein in the extracellular matrix, collagen (COL) plays a key role in bone tissue engineering [15]. As the most prevalent protein in mammals, COL establishes a structural network in almost all tissues owing to its high degree of polymorphism, which leads to the production of a wide variety of different configurations of it. Natural bone is made up of COL fibrils that are mineralized by calcium phosphate components identical to those seen in hydroxyapatite (HA) [16]. In addition to its high-water affinity, collagen is an excellent biomaterial because of its controlled biodegradation, hemostatic properties, minimum inflammation host immune response, biocompatibility and the capacity to help cellular adhesion. This makes COL an excellent material for creating bone tissue because of its structural stability, which may be used to provide a template for the accumulation of calcium phosphate ($Ca_3(PO_4)_2$) and calcium carbonate ($CaCO_3$) in the bone [17]. However, collagen seems to lack mechanical strength and stiffness, both of which are necessary for cell culture assays in vitro and in vivo implantation, because structural functioning, as well as biophysical (mechanical) stimulation, are needed. This drawback can be solved by using silk fibroin (SF) and collagen combined in the fabrication of the composite fiber matrix for the bone tissue engineering scaffold's backbone. Silk fibroin (SF) is a protein that is readily accessible in nature and is mostly made of amino acids such as glycine, alanine, and serine. The extraction and purification of silkworm cocoons may result in the production of SF substance as a byproduct. As a result of its exceptional biological compatibility and superior mechanical properties, SF is an ideal material for use in bone regeneration procedures. By altering the quantity of β-sheet present in SF, it is possible to adjust the degradation rate and mechanical properties of the material. However, since the manufacturing temperature of SF solution in an aqueous medium is near to the temperature of the normal human body, it can be helpful to load a variety of cells or biological components under mild conditions [18]. An earlier study conducted by Zhang et al. used electrospinning methods to create SF scaffolds that were loaded with vascular endothelial growth factor (VEGF) [19]. This composite scaffold has excellent mechanical properties as well as excellent biocompatibility, which may result in beneficial results in the field of bone tissue repair.

Furthermore, the scaffold with controlled bone regeneration, biocompatible, spatial, accessible to fluids, bioabsorbable, bone-promoting, antibacterial capabilities, and economically affordable was prepared by electrospinning techniques [20]. In the recent two decades, numerous researchers have been more interested in the manufacturing of nanofibers for bone tissue engineering applications. They create nanofibers using a variety of methods, including self-assembly [21], phase separation [22], vapor phase polymerization [23] and electrospinning [24]. When it comes to creating nano-fibrous scaffolds, the electrospinning approach is a convenient option that has been frequently used. They closely resemble extracellular matrix (ECM) in terms of mechanical properties, porosity, and surface area to volume ratio. This promotes improved cell adhesion and spreading as well as growth and proliferation [30]. Introducing specified biomolecules and nanostructures into a polymeric solution will provide an electrospun scaffold with functionality. Electrospun fibers, parameters such as voltage, rollers rotating speed, the viscosity of the injected solution, injection rate and needle to collector distance can be adjusted to tune the porosity and fiber diameter [25]. Core-shell nanofibers are made with a particularly unique coaxial electrospinning technique that utilizes a combination of two different polymer solutions [26]. When used as a drug carrier, electrospun nanofibers have an advantage over other nanocarriers such as micelles, hydrogels, nanoparticles and so on because they can encapsulate more medicines into the scaffold. Nanofibers have also shown a prolonged drug release, conserving the bioavailability of active pharmaceuticals such antioxidants, oligopeptides, antibiotics, medicinal components and growth factors [27]. Distinct drug loading procedures lead to varied forms of interactions between pharmaceuticals and nanofibers, detecting different drug-releasing kinetics [28].

In this approach, we were able to fabricate the mineralized composite nanofiber scaffold with the aid of electrospinning techniques, which may be employed to increase osteogenic bone repair expression in osteoporosis treatment. The incorporation of collagen, silk fibroin, and bioactive glass nanoparticles (CaO-SiO_2) to create COL/SF/CaO-SiO_2 composite nanofiber, which was inspired by the hybrid structure of the animal bone matrix. The physicochemical, morphological, and functional characterization was further investigated in order to confirm the successful formation of the COL/SF/CaO-SiO_2 composite nanofiber. According to the research, this bioinspired mineralized composite nanofiber may be able to mimic the nanoscale structure and chemical composition of natural bone minerals. Additionally, COL/SF/CaO-SiO_2 has exceptional stability, biocompatibility, bioactivity, osteoconductivity, and is non-toxic. In a laboratory context, we demonstrated that our bioinspired mineralized composite nanofiber may act as a favorable microenvironment for osteoblast formation. Additionally, in-vitro research revealed that CaO-SiO_2 nanoparticles inherited COL/SF/CaO-SiO_2 potentials to induce osteogenesis and differentiation. The mineralized composite nanofiber was implanted into the bone defects in the tibia of osteoporotic Wistar rats to further investigate their in-vivo bone regeneration potential. After 12 weeks of therapy, it was observed that the mineralization composite nanofibers aided in the regeneration of bone in osteoporotic bone defects. These findings indicated that the COL/SF/CaO-SiO_2 scaffolds produced for the repair of osteoporotic bone defects had the potential to be employed in the future.

2. Materials and methods

2.1. Reagents and chemicals

The silk cocoons of *Bombyx mori* used in this study were obtained from the Zhejiang province of China. Dialysis membrane with pore size 12 kDa MWCO and Masson-Goldner staining kit was purchased from Fisher Scientific Pvt. Ltd. China. Saos-2 (Sarcoma osteogenic) cell lines were obtained from Xiaoshan Traditional Chinese Medical Hospital. Zhejiang Province, China. The analytical grade sodium carbonate (Na_2CO_3), lithium bromide

(LiBr), cetrimonium bromide (CTAB), liquid ammonia (NH_4OH), calcium nitrate tetrahydrate ($Ca(NO_3)2.4H_2O$), tetraethyl orthosilicate ($Si(OC_2H_5)_4$), ethanol (CH_3CH_2OH), acetic acid (CH_3COOH), polyvinyl alcohol (PVP, molecular weight: 89,000–98,000), sodium chloride (NaCl), magnesium chloride ($MgCl_2.6H_2O$), calcium chloride ($CaCl_2.2H2O$), hydrogen peroxide (H_2O_2), were purchased from Sigma- Aldrich. Ltd. China. The biochemical reagents such as glutaraldehyde ($OHC(CH_2)_3CHO$), minimum essential medium (α-MEM), fetal bovine serum (FBS), streptomycin solution ($C_{21}H_{39}N_7O_{12}.1.5H_2SO_4$), penicillin-streptomycin, trypsin, ethylenediaminetetraacetic acid (EDTA), 3-(4,5-dimethylthiazol-2-yl)-2,5-diphenyl tetrazolium bromide (MTT), dimethyl sulfoxide (DMSO), monosodium phosphate ($C_{10}H_8NaO_4P$), chloral hydrate solution ($C_{13}CCH(OH)_2$), hematoxylin ($C_{16}H_{14}O_6.xH_2O$), eosin B ($C_{20}H_6N2O9Br2Na2$), 3,3′-Diaminobenzidine ((NH2) 2C6H3C6H3(NH2)2) were supplied by Himedia and Sigma-Aldrich. Pvt. Ltd. (China). Deionized water has been used in all the experimental sections.

2.2. Fabrication of COL/SF/CaO-SiO_2 composite nanofiber scaffolds

2.2.1. Preparation of silk fibroin solution from Bombyx mori silk cocoon

Sericin, a hydrophilic gum-like protein, bound the fibroin fibers in the *Bombyx mori* silk cocoon. A silk cocoon's sericin is usually removed following fibroin is extracted. Many methods exist to extract and purify silk fibroin. Degumming is a common method for eliminating sericin. *Bombyx mori* silk cocoons were sliced into small pieces and boiled with 0.2 M aqueous solution of Na_2CO_3 at 100 °C for 30 min, stirring continually. Rinse with deionized water to remove glue-like sericin and dry at room temperature. Extraction of silk fibroin occurs by dissolving the aforementioned solution in 9.3 M lithium bromide (LiBr) at 70 °C. After the silk fibroin-LiBr solution was dialyzed with the aid of semipermeable membrane (12 kDa MWCO) against deionized water for 72 h at room temperature to eliminate excess LiBr salt. It was then centrifuged for 10 min at 6000 rpm to remove any leftover contaminants and kept at 4 °C for future processing [29].

2.2.2. Preparation of bioactive glass (CaO-SiO_2) nanoparticles

The sol-gel technique was employed to manufacture the bioactive glass nanoparticles (BAGNPs), with a Ca: Si molar ratio of 25:75 being used to make the nanoparticles. In this process, cetrimonium bromide (CTAB) solution was added to a suitable quantity of ammonia solution to bring the pH of the solution up to 12.5 throughout this procedure. Following that, the calcium nitrate tetrahydrate $Ca(NO_3)_24H_2O$ was employed to dissolve into the solution. Additionally, tetraethyl orthosilicate ($SiC_8H_{20}O_4$) was dissolved in 100% ethanol prior to being added to the above solution and agitated with ultrasonics for 20 min. After that, the solution was put in a magnetic stirrer overnight to ensure that the reaction had been completed successfully. The obtained precipitate was centrifuged at 3000 rpm for 10 min and dried at 90 °C for 24 h. Then, the CaO-SiO_2 powders were calcined at 1000 °C for 2 h at a rate of 5 °C/min.

2.2.3. Fabrication of COL/SF/CaO-SiO_2 composite nanofibers by electrospinning techniques

The electrospinning technique was employed to create a COL /SF/CaO-SiO_2 composite nanofiber, as seen in Fig. 1. COL and SF were dissolved in acetic acid in a 3:1:1 ratio, followed by a few milliliters of water additions. The solution was then heated to 60 °C and a little quantity of PVA was added while constantly stirring for 5 h. PVA enhances the viscosity of composite solutions significantly. Following that, the color of this solution was altered from light yellow to orange, indicating that a homogenous COL/SF solution had been formed successfully. After crosslinking with glutaraldehyde, this solution was employed in electrospun procedures. To produce the composite solution, 1g of previously prepared CaO-SiO_2 bioactive glass nanoparticles (BAGNPs) were added to the COL/

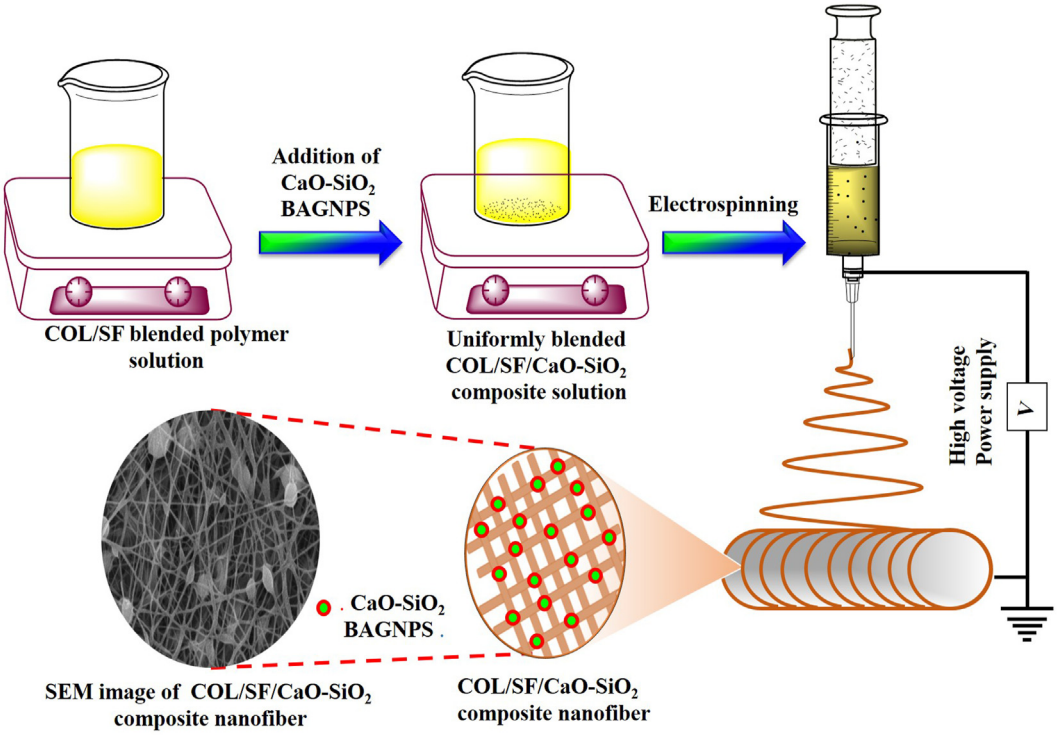

Fig. 1. Schematic representation of the fabrication process of COL/SF/CaO-SiO_2 composite nanofiber.

SF polymeric solution and agitated for 30 min while maintaining a constant temperature of 70 °C. Following that, a 10 mL syringe equipped with a 0.7 mm stainless-steel needle was used to inject the COL/SF/CaO-SiO_2 composite polymeric solution at a rate of 0.7 mL/h. Electrospinning is performed with the drum collector rotating at 1200 rotations per minute and the syringe 10 cm distant from the drum. Additionally, aluminum foil was employed to cover the drum collector's surface to help in the extraction of nanofibers. The electrospinning process started with a high voltage being applied to the polymer solution (21 kV). Due to the high voltage, the polymer matrix self-aligns into a nanofiber. The resulting nanofibers (COL/SF and COL/SF/CaO-SiO_2) were recovered from an aluminum foil and dried at room temperature prior to further analysis. The COL/SF nanofiber was fabricated in this technique without the inclusion of CaO-SiO_2 BAGNPs in order to compare their physicochemical and biomedical characteristics to those of the COL/SF/CaO-SiO_2 composite nanofiber.

2.3. Characterization of nanofibers

The nanofibers were produced using the Espin Nano(V2HC2) electrospinning device. The crystalline nature of the synthesized COL/SF and COL/SF/CaO-SiO_2 composite nanofibers were investigated using the X-ray diffraction (XRD) technique (X'pert PRO analytical diffractometer) with Cu-K radiation ($\lambda = 1.541$). The morphology and composition of the electrospun composite nanofiber tubular scaffold were investigated using a Hitachi S-4700 scanning electron microscope (SEM) equipped with energy-dispersive X-ray spectroscopy (EDX) at a 15 kV applied potential. Additionally, utilizing a JEM-2010F-TEM (JEOL, Japan) at 200 kV, high-resolution transmission electron microscopy (HR-TEM) was employed to explore the detailed investigation of surface morphology and doped BAG nanoparticle size and shape. Image J software was used to resolve the SEM and HR-TEM micrographs in order to identify the precise size of nanofibers and BAG nanoparticles. The attenuated total reflection (ATR) mode of Fourier Infrared spectroscopy (FTIR) with the JASCO-4600 (Perkin Elmer) was utilized to analyze the functional groups present in the composite nanofiber with a wavenumber of 4000-400 cm^{-1}. Atomic force microscopy (AFM) using the Nanosur-Easy scan 2 (Switzerland) was used to measure the surface smoothness and thickness of the nanofibers. The elements and their bonding states in the composite nanofiber were analyzed using the PHI - VersaProbe III – X-ray photoelectron spectroscopy (XPS). Curve fitting of the XPS data was performed using the Casa-XPS program. The thermal stability and decomposition of nanofibers were examined using thermogravimetric analysis (TGA) using PerkinElmer STA-6000 analytical instruments. The tensile strength and elongation break of the fabricated nanofiber were measured in a universal testing machine model (Tinnitus Olsen Horizon) at room temperature. It predicts that the inclusion of silk fibroin and bioactive glass (CaO-SiO_2) nanoparticles would improve the mechanical properties of the collagen fiber scaffold.

2.4. MTT assay procedure for determining the in vitro biocompatibility of COL/SF/CaO-SiO_2 composite nanofiber against osteoblast cells

2.4.1. Cell culture

In cell culture experiments, using the Saos-2 (Sarcoma osteogenic) cell line was used to assess the biocompatibility of the Fabricated nanofiber. Minimum Essential Medium (α-MEM) was used to cultivate the Saos-2 cells, which was supplemented with 10% diluted fetal bovine serum (FBS) and 1% streptomycin/penicillin to achieve the desired results. The cell culture that was created was kept for 24 h at 37 °C in a humidified environment with a 5.0% CO_2 flow in a humidified atmosphere. It was customary for the cultural media to change every three days. As a consequence, a solution containing 0.5% trypsin and 0.05% EDTA solution was employed to sustain the Saos-2 cells that had been cultured.

2.4.2. Biocompatibility

In order to determine whether or not fabricated nanofibers were biocompatible with Saos-2 cells, an MTT assay was performed. Initially, the Saos-2 cells were diluted with 1:100 in sterile culture media and 2×10^4 cells/well were cultivated in the 24-well plate for 1, 3, and 7 days with the addition of tested materials (COL/SF and COL/SF/CaO-SiO_2 composite nanofiber). Then, the treated Saos-2 cells were taken out and rinsed with PBS solution at the end of the seven-day period. At 37 °C for 5 h, 100 μL of Saos-2 cells were added to 100 μL (12.5 mg/mL) of MTT (3-(4,5-dimethylthiazol-2-yl)-2,5-diphenyltetrazolium bromide) solution, to create MTT formazan, and then the reaction was incubated to complete the formation of MTT formazan. To liquefy the formazan, 400 μL of dimethyl sulfoxide (DMSO) was added to the growth media and sonicated for 10 min. Finally, the viability or biocompatibility of the cells was assessed using a UV-Vis spectrophotometer to determine the optimal density (OD) of MTT solution at 570 nm (JASCO-V530). The control was made up of just the culture medium and not any of the tested samples. The percentage (%) cell viability was calculated from the OD (optimal density) measured by a microplate reader at 570 nm using the formula below (1).

$$\%\ \text{Cell viability} = \frac{Mean\ OD_{570nm}\ \text{Treated Cells}}{Mean\ OD_{570\ nm}\ \text{Control Cells}} \times 100 \qquad (1)$$

The cell adhesion ability of the fabricated (COL/SF and COL/SF/CaO-SiO_2) composite nanofiber was tested with the aid of the above-mentioned 7-day treated Saos-2 cells. After being incubated with the fabricated composite nanofiber, they were withdrawn from the culture medium and washed three times with PBS buffer solution (pH 7.4) before being fixed on the sampling surface with 2.5% glutaraldehyde at 4 °C for 30 min. As a result, the cells were dried with ethanol and been freeze-dried. Finally, the samples were allowed to air dry and examined under a scanning electron microscope (SEM) to assess the nature of cell attachment [30].

2.5. In-vivo animal studies for the treatment of osteoporosis in Sprague Dawley rats

2.5.1. Preparation and mineralization of COL/SF and COL/SF/CaO-SiO_2 bone cement

The COL/SF and COL/SF/CaO-SiO_2 bone cement were made by mixing the COL/SF and COL/SF/CaO-SiO_2 composite nanofiber with ionic water at a ratio of 1:0.5, respectively. The bone cement was then dried in a vacuum oven set to 60 °C once it had finished drying. Bone cement made with the COL/SF and COL/SF/CaO-SiO2 were placed in simulated body fluids (SBF) comprising 100 mM sodium chloride (NaCl), 0.5 mM magnesium chloride ($MgCl_2$), 1 mM monosodium phosphate (NaH_2PO_4), 1 mM sodium bicarbonate (Na_2CO_3), and 2.5 mM calcium chloride (Ca_2CO_3) at 37c for 7 days before being tested. After that, the bone cement was thoroughly washed with ultrapure water three times and dried at 60 °C to eliminate any remaining SBF.

2.6. In vitro degradation

After being a fabrication of bone cement with the aid of CaO-SiO2 bioactive nanoparticles and COL/SF/CaO-SiO2 composite nanofiber, it was degraded in-vitro in a 37 °C thermal oscillator. The

supernatants were collected at various time intervals (1day, 3days, 1week, 2weeks, 4weeks, 6weeks, and 12weeks), and the Ca^{2+} and Si^{4+} concentrations in the supernatants were measured using Inductively Coupled Plasma-Mass Spectrometry (ICP-MS - Discover the NexION 5000, PerkinElmer). After the supernatant was removed by centrifugation, then dried and weighed bone cement was used to quantify the weight loss of bone cement at different degradation time points.

2.7. Creation of osteoporosis rat model

Sprague Dawley (SD) rats weighing 200–250g were used. The osteoporosis model was created via the bilateral ovariectomy (OVX) surgical procedure. In summary, female rats had their bilateral ovaries removed and ligated, and they were subsequently given a calcium-deficient diet for four weeks. After validating the osteoporotic rats' condition using the Lunar Prodigy dual-energy X-ray absorptiometry system (Germany), a crucial bone defect construct sized 5 mm in length and 3 mm in diameter was constructed. The ovariectomized rats with bone defects were then randomly assigned to one of three groups: a control group that received no therapy, a group that received COL/SF scaffold treatment, or a group that received COL/SF/CaO-SiO_2-treated.

2.7.1. Implantation of COL/SF and COL/SF/CaO-SiO_2 scaffold into the femoral defect of OVX rats

During this process, Rats were anesthetized with 4% chloral hydrate (1mL/100 g) solution and disinfected with iodophor and 75% ethanol prior to the surgery. The incision was about 2 cm long, and the tissue and fascia on the tibia's surface were retracted to reveal the surgery site. On the tibial plateau, a defect 3 mm in diameter and 5 mm in length was created using a 3 mm dental grinding drill. After the defect was successfully formed, the bone fragments and blood in the defect region were completely cleaned, and the defect area was implanted with irradiation sterilized bone cement. Finally, the wound was sutured in layers, the region around the incision cleaned with iodophor, and the rats were injected with penicillin at a rate of 800,000 units/day for three days after surgery. The rats were placed on a regular diet 12 weeks following surgery. Rats treated with COL/SF and COL/SF/CaO-SiO_2 were killed 6 and 12-weeks following surgery, and the tibia was removed and preserved in a 4% formalin solution for future study.

2.7.2. Histological immunohistochemical staining

Following treatment, the samples were immersed in a 10% EDTA solution to decalcify them until the needlepoint pierced the bone smoothly. After drying the defect and surrounding area with rising grades of alcohol and embedding them in paraffin, they were preserved. Longitudinal sections from each specimen were cut into 150 mM thick slices and stained with hematoxylin and eosin (H&E) and Masson-Goldner. Three slices of each rat were analyzed using a fluorescence microscope (Olympus, IX73, Japan). Before immunohistochemical labeling, the deparaffinized slides were rehydrated and then submerged in hydrogen peroxide to quench the peroxidase. Before incubating with the primary antibodies against OCN, CD31 and OPG, the slides were treated with 5–10% of bovine serum albumin (BSA). After 1–2 h of incubation, the slides were treated for 10–30 min at 37 °C with the biotinylated secondary antibody (1% BSA-PBS solution dilution). Then, streptomyces ovalbumin linked with horseradish enzyme (prepared by diluting in PBS) was incubated for 10–30 min. Staining with 3,3′-diaminobenzidine (DAB), counterstaining with hematoxylin, and sealing with neutral gum were used on the slides. The slides were examined using a light microscope.

3. Results and discussion

3.1. XRD analysis: crystallographic properties of composite nanofiber

The crystallographic properties of the fabricated nanofiber were investigated using X-ray diffraction (XRD) analysis, and the results are shown in Fig. 2 a. The XRD pattern of the electrospun

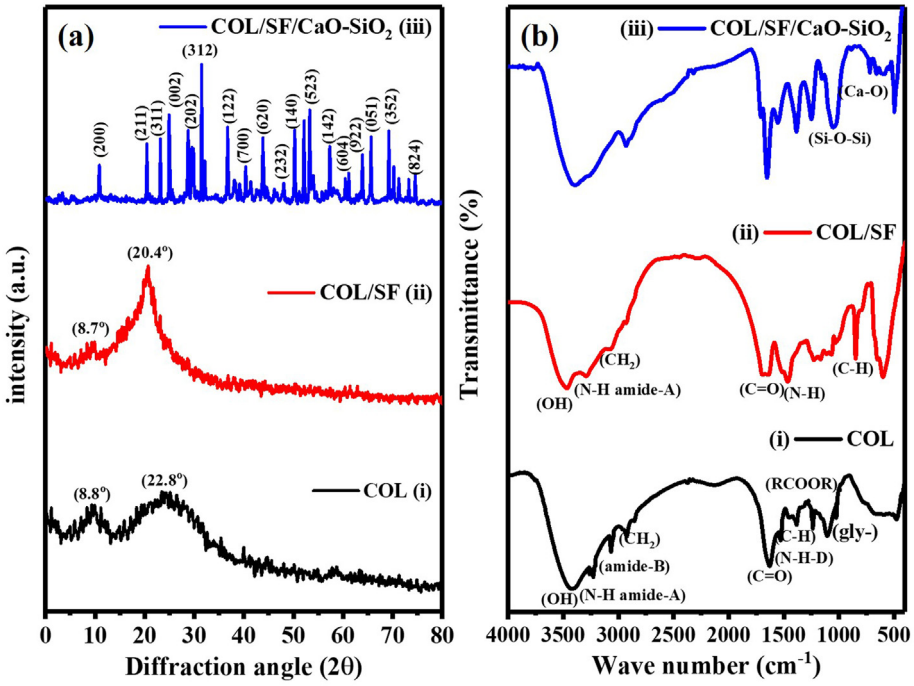

Fig. 2. (a) XRD and (b) FTIR spectrum of COL (i), COL/SF (ii) and COL/SF/CaO-SiO_2 (iii) composite nanofiber.

collagen (COL) fiber displays (Fig. 2 a.i) the characteristic peaks of COL, with a small diffraction peak at about 8.8° (P1) and a broad peak at around 22.8° (P2), indicating that the collagen sample is amorphous in nature [31,32]. The d-spacing of the COL fiber is estimated from the 2θ value and is found to be 1 nm and 0.39 nm for P1 and P2, respectively. There is information in the d-spacing value concerning lamellar layer thickness as well as the average inter-chain distance of the COL macromolecule in the fibers. The COL/SF composite nanofiber XRD pattern (Fig. 2 a.ii) shows two notable peaks around 2θ at 8.7° and 20.4°. The incorporation of silk fibroin (SF) fibers on the surface of COL resulted in the suppression of P1 and P2 peaks, with the P1 peak shifting towards 2θ = 8.7° and a d-spacing of 1.02 nm for COL/SF nanofiber [33]. The SF/COL fiber has a peak around 2θ = 20.4°, which is the primary peak of SF and is attributed to amino acid sequences and conformations. Most glycine-X repeats encompass 94% of the silk sequence (X is the repetition unit of alanine, serine and tyrosine with 65%, 23% and 9% respectively) predominantly form crystalline domains in SFs, resulting in the crystalline peaks [34]. In addition, the XRD pattern of COL/SF/CaO-SiO_2 ((Fig. 2 a.iii) composite nanofiber exhibits the diffraction peaks at 11.23, 20.46, 23.36, 25.10, 28.58,

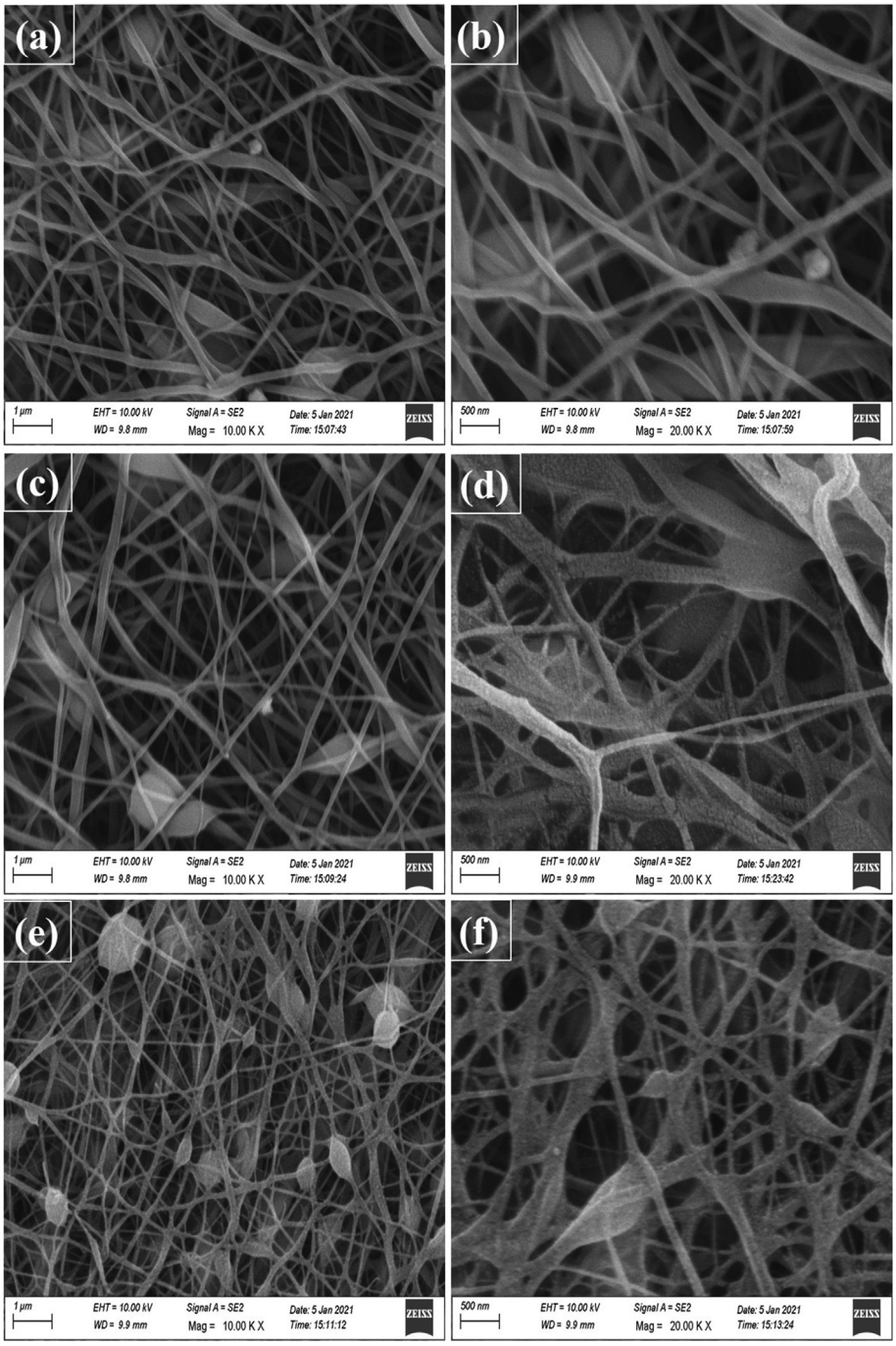

Fig. 3. SEM micrographs of COL (a & b), COL/SF (c & d) and COL/SF/CaO-SiO_2 (e & f) composite nanofiber.

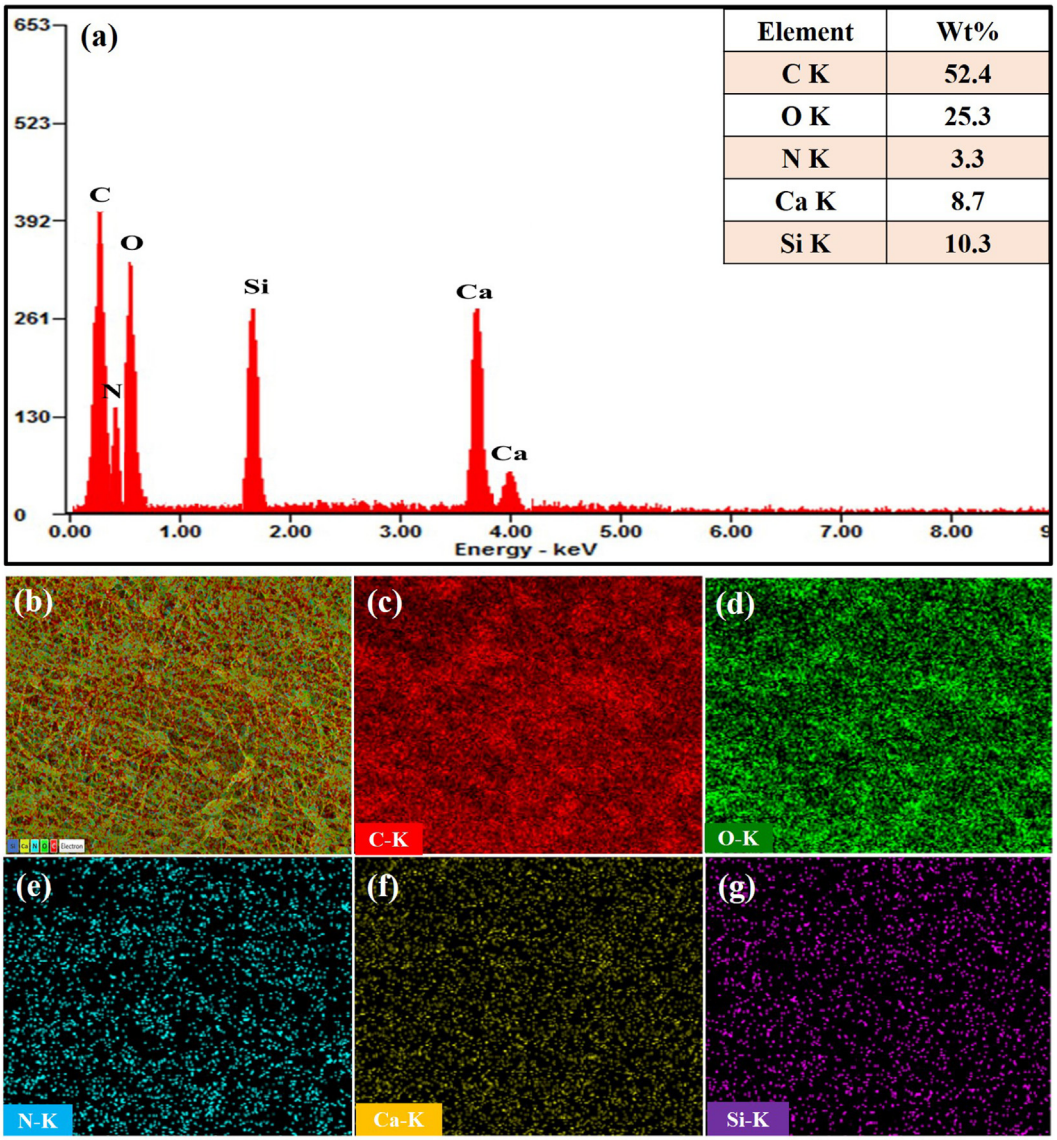

Fig. 4. EDX spectrum (a) and EDX color mapping: overall mapping (b), carbon (c), oxygen (d), nitrogen (e), calcium (f) and silicon (g) in the COL/SF/CaO-SiO_2 composite nanofiber.

31.48, 36.70, 40.17, 43.65, 47.71, 50.32, 52.35, 53.51, 57.27, 60.75, 63.94, 65.68, and 74.67 corresponding to the (200), (211), (311), (002), (202), (312), (122), (700), (620), (232), (140), (204), (523), (142), (604), (922), (051) and (824) lattice plane of CaO-SiO_2 bioactive glass nanoparticles (BAGNPs) exist in the composite fiber matrix. The observed findings are well-matched with the standard CaO-SiO_2 JCPDS file No: 10–0489 and confirm the formation of wollastonite crystals [35]. The average crystalline size of CaO-SiO_2 BAGNPs in COL/SF/CaO-SiO_2 composite fiber was calculated using the Debye–Scherer formula and was found to be about 37 nm. The CaO-SiO_2 high-intensity crystalline peak suppressed the COL and SF peaks. As a result, there are no recognizable COL and SF crystalline peaks in the XRD pattern of the COL/SF/CaO-SiO_2 composite fiber matrix. The presence of certain noisy peaks supports the presence of COL and SF in the composite fiber matrix. These findings support the crystallinity of CaO-SiO_2 BAGNPs and confirm the successful formation of COL/SF/CaO-SiO_2 composite fiber.

3.2. FTIR analysis: functional group identification of composite nanofiber

Fourier transform infrared spectroscopy (FTIR) was used to investigate the functional groups present in collagen (COL), silk fibroin (SF), and bioactive glass (BAG) nanofibers, as well as their interaction of bonding vibrations, in the attenuated total reflection (ATR) mode and the wavenumber range 4000 to 400 cm^{-1}. For every produced nanofiber, the largest wide peak for the OH group was detected between 3500 and 3200 cm^{-1}. FTIR spectra revealed that collagen contains a rich protein fibrous structure with substantial amide I, II, III and amide A, B functional group characteristics [36,37]. The existence of all of this functional group in our sample was verified by the distinctive band position. The band at 3277 cm^{-1} in the COL FTIR spectrum (Fig. 2 b.i) corresponds to N–H stretching of amide A functionalities. Furthermore, the bands at 3059 and 2914 cm^{-1} are assigned to the amide B functional group. The band at 1639 cm^{-1} is attributed to C=O stretching of amide I,

whereas the band at 1531 cm-1 is attributed to N–H deformation of amide II. The distinctive bands of C–H bending and carboxyl groups are located at 1462 and 1373 cm^{-1}, respectively. The band at 1226 cm^{-1} confirms the N–H deformation of amide III. The ester bond and glycoside linkage are responsible for the bands at 1080 cm^{-1} and 1026 cm^{-1}, respectively. The peak at 2911 cm^{-1} is due to the stretching vibration of CH_2. The stretching vibration of intermolecular hydrogen bonds (O-H group) is reflected in the FTIR spectrum of COL/SF (Fig. 2 b.ii), and the stretching vibration of CH_2 is reflected in the absorption at 2931 cm^{-1}. In silk fibroin and gelatin, the amino groups include polypeptide (-CONH-) connections, which are visible in the FTIR spectrum. Peaks at 1665, 1524 and 1273 cm-1 correspond to the stretching vibrations C═O, N-H bending vibration, and C-N stretching vibration, respectively. Furthermore, at 850 cm^{-1}, the C-H stretching vibration was discovered. According to the findings, the COL/SF nanofiber comprises amino groups with peptide connections [38]. The FTIR spectra of COL/SF/CaO-SiO_2 composite nanofiber (Fig. 2 b.iii) show similar peaks to their counterparts (C═O, C-N, N-H, C-H peaks of COL and SF matrix). Furthermore, the composite nanofiber has additional peaks at 1082 and 489 cm^{-1} that corresponds to Si-O-Si stretching and bending vibrations, respectively, and a peak at 719 cm^{-1} that depicts Ca-O stretching vibration. The peak at about 1369 cm^{-1} suggests the establishment of a chemical connection between the amide groups of COL/SF and the Ca^{2+} ions of BAG nanoparticles [39,40]. The aforementioned findings support the synthesis of bioactive glass nanoparticles and their interaction with COL/SF composite nanofiber.

3.3. SEM with EDX analysis: examination of morphology and elemental composition of composite nanofiber

The surface morphology of composite nanofibers and the different shapes and diameters of nanoparticles anchored on the composite nanofiber matrix were studied using the scanning electron microscope (SEM) technique. A needle with beadles and a fiber matrix are seen in SEM images of COL (Fig. 3a & b). The fiber matrix in the COL has an average diameter of 119.45 ± 10 nm. SEM micrographs of the COL/SF composite nanofiber (Fig. 4c & d) show a random and well-framed beta-sheet structure. Tube structure in fiber matrix is also around 114.97 ± 10 nm in diameter. Fig. 3e & f shows that the COL/SF/CaO-SiO_2 composite nanofiber has a needle-like structure with an average diameter of 105.63 ± 10 nm, with bead-like structures on both sides of the fiber. Bioactive glass (CaO/SiO_2) nanoparticles are clearly visible in this micrograph.

EDX spectroscopy was used to examine and map the components contained in the COL/SF/CaO-SiO_2 composite nanofiber (Fig. 4a). The obtained results (Fig. 4. (a) inset) confirmed that carbon made up 52.4% of the K type series, oxygen made up 25.3% of the K type series, nitrogen made up 3.3% of the K type series,

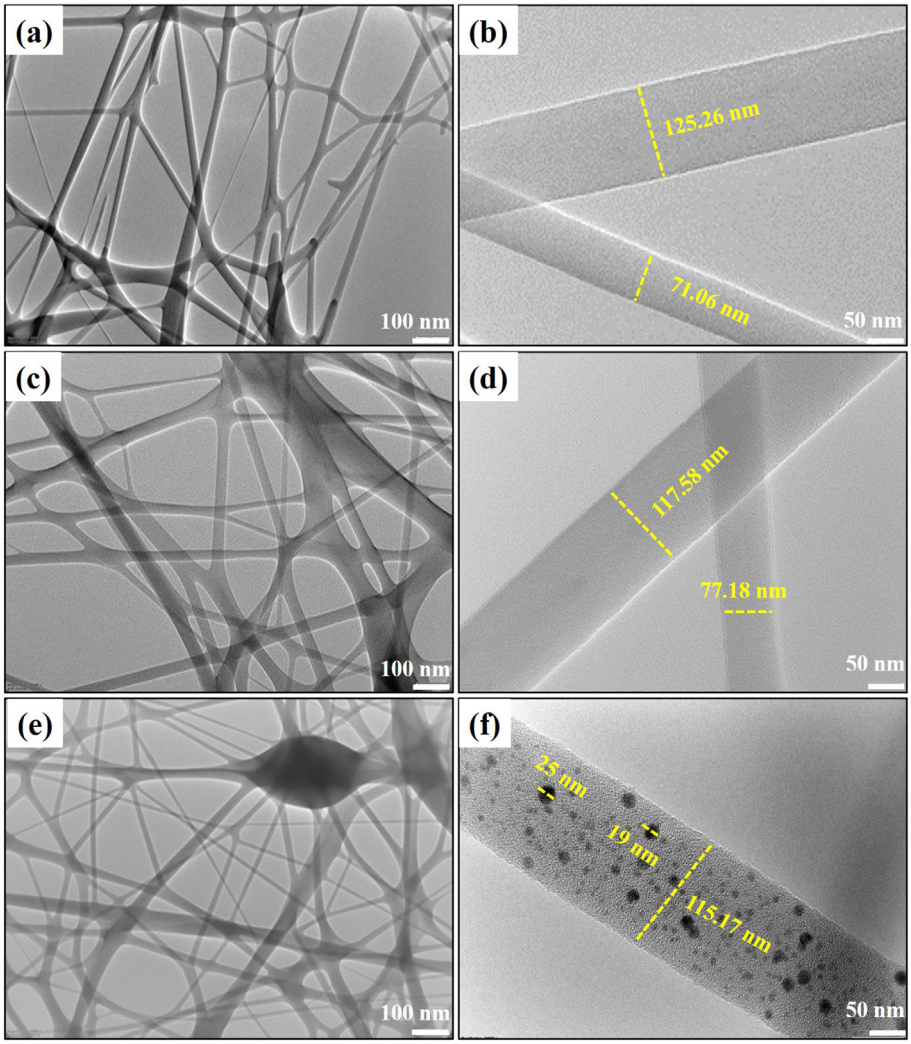

Fig. 5. HR-TEM micrographs of COL (a & b), COL/SF (c & d) and COL/SF/CaO-SiO_2 (e & f) composite nanofiber with different (100 nm and 50 nm) magnification.

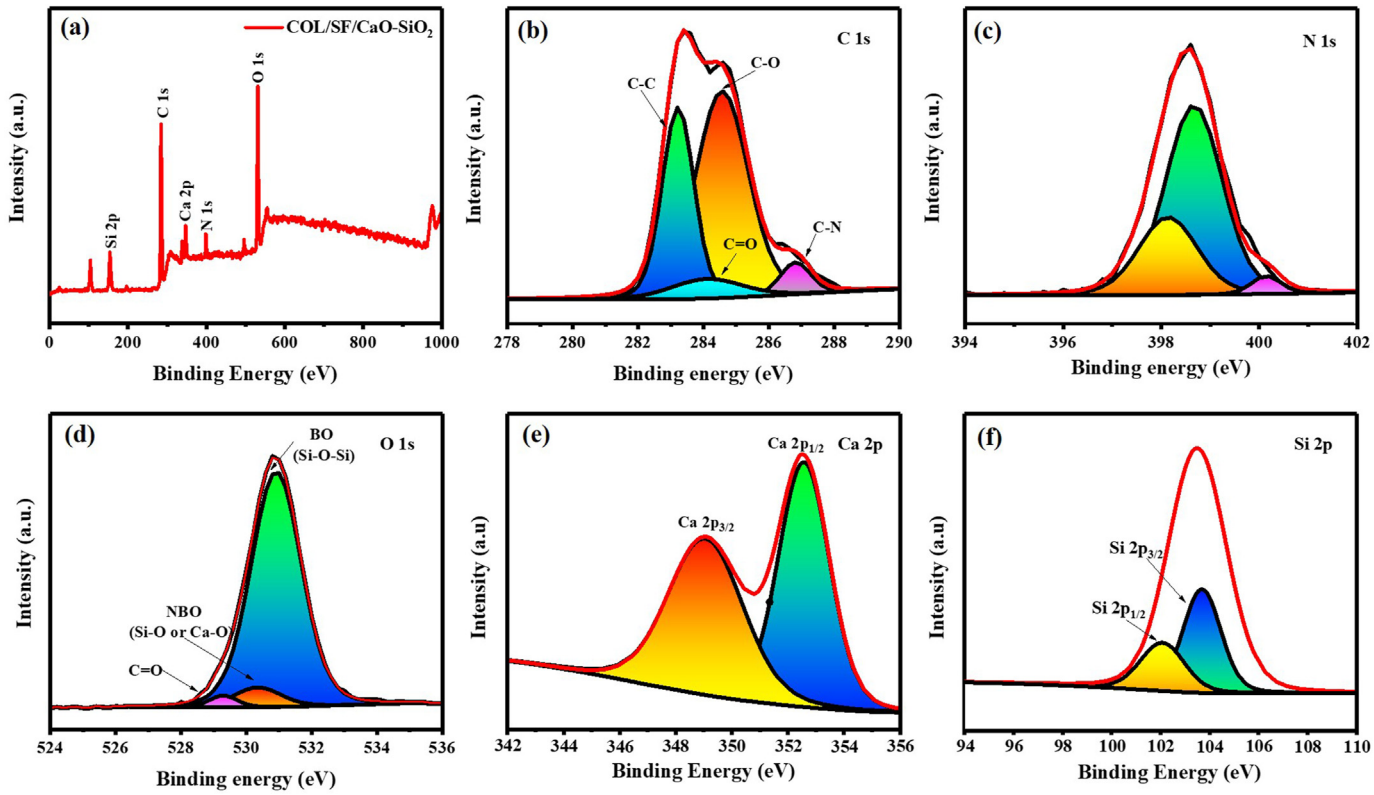

Fig. 6. XPS survey spectrum of COL/SF/CaO-SiO_2 composite nanofiber (a) and corresponding high-resolution XPS survey spectrum of C 1s (b), N 1s (c), O 1s (d), Ca 2p (e), and Si 2p (f).

Table 1
The results obtained from the overall XPS spectrum of COL/SF/CaO-SiO_2 composite nanofiber.

Name	Position (eV)	FWHM	Area	At%
C 1s	284.00	3.39	110432.23	59.46
N 1s	398.00	2.71	11026.33	3.30
O 1s	531.00	2.86	110223.94	20.25
Ca 2p	347.00	2.76	31866.89	3.38
Si 2p	104.00	3.0	20649.87	13.61

calcium made up 8.70% of the K type series, and silicon made up 10.3% of the K type series. In addition, the EDX color mapping was tested to establish its elemental combination and occurrence in the composite matrix. The colored micrographs of the COL/SF/CaO-SiO_2 composite nanofiber (Fig. 4b) show how each constituent in the fiber matrix is distinct. Carbon is represented by the red color in this mapping (Fig. 4c), oxygen by the green color (Fig. 4d), nitrogen by the blue color (Fig. 4e), calcium by the light-yellow color (Fig. 4f), and silicon by the purple color (Fig. 4g). The existence and equal distribution of carbon (C), oxygen (O), nitrogen (N), calcium (Ca), and silicon (Si) in the composite fiber matrix were verified by the above results.

3.4. HR-TEM analysis: Identification of internal structure, shape and size of the composite nanofiber

The internal structure of a composite nanofiber, as well as the size and shape of nanoparticles, were studied using high-resolution transmission electron microscopy (HR-TEM). The nanofiber was electrospun directly onto a carbon-coated copper grid before being studied with a TEM. The micrographs in this surface study are displayed in various magnifications for comprehensive assessment, such as 100 nm and 50 nm. The COL nanofiber has a core-shell net structure with a rod shape morphology, as revealed in the TEM micrographs (Fig. 5. (a, b)). The nanofiber has an average diameter of around 125 ± 10 nm. The TEM micrographs of the COL/SF composite nanofiber (Fig. 5. (c & d)) indicated a rod-shaped morphology with a diameter of 117 ± 10 nm. TEM micrographs of the COL/SF/CaO-SiO_2 composite nanofiber (Fig. 5. (e & f)) indicated that the fibers were organized in a stick with rod shape morphology with a diameter of 115 ± 10 and that bioactive glass (CaO-SiO_2) nanoparticles with a size of 20 ± 5 nm were detected on the fiber matrix's surface. These findings indicated the presence of evenly dispersed CaO-SiO_2 nanoparticles anchored on the surface of the fiber matrix. Furthermore, the morphology acquired via the TEM study was almost comparable to that obtained by SEM analysis. Both results indicated the creation of a composite nanofiber with the specified size and shape.

3.5. XPS analysis: investigation of elemental composition and electronic state of the element present in the composite nanofiber

The electronic states of each element contained in the composite nanofiber were analyzed using X-ray photoelectronic spectroscopy (XPS) by measuring binding energy. The wide survey XPS spectrum of COL/SF/CaO-SiO_2 (Fig. 6 a.) exhibits peaks associated to C1s, N1s, O1s, Ca2p, and Si2p elements with binding energies of 284.00eV, 398.00eV, 531.00eV, 347.00eV, and 104.00eV, respectively [41]. The atomic percentages of all elements were estimated using the full-width half maximum of the relevant peaks in the XPS spectra. According to this analysis, carbon has an atomic percentage of 59.46%, nitrogen has an atomic percentage of 02.71%, oxygen has an atomic percentage of

20.25%, calcium has an atomic percentage of 3.38%, and silicon has an atomic percentage of 13.61% (Table 1). The high-resolution C1s spectrum (Fig. 6b) was multiplied by four separate peaks representing C-C, C-O, C-N, and C═O with binding energies of 283.19eV, 284.60eV, 286.81eV, and 284.16eV, respectively. These peaks were created by carbons in amino acids (C-O-C, C-N, and C═O) as well as sp^2, sp^3 hybridized carbons (C-C) in collagen and silk fibroin [42,43]. The high-resolution N1s spectrum (Fig. 6c) was separated into three peaks for different nitrogen present in amino acids, including Glycine-Gly-N, Alanine-Ala-N, and Serine-Ser-N. All of these amino acids are substantially accumulated to collagen and silk fibroin, with Gly-N peak at 398.06eV, Ala-N peak at 398.76eV, and Ser-N peak at 399.05eV [44]. The high-resolution O1s spectrum (Fig. 6d) was further subdivided into three peaks at 531.01eV, 530.04eV, and 529.27eV, which correspond to the bridging oxygen (Si-O-Si), non-bridging oxygen (Si-O or Ca-O), and C═O bonds in the polymer matrix's carbonyl functional group. The Ca2p high-resolution spectrum (Fig. 6e) was further subdivided into two peaks at 349.80eV and 351.55eV, which correspond to the $Ca2p_{1/2}$ and $Ca2p_{3/2}$ metallic states, respectively. These two peaks indicate the CaO nanoparticles at Ca^0 and Ca^{2+} oxidation states. Finally, the Si2p high-resolution XPS spectrum (Fig. 6f) was divided into two peaks for $Si2p_{1/2}$ and $Si2p_{3/2}$ metallic states, which are Si^0 and Si^{4+} in this oxidation state with binding energies of 101.95eV and 103.92eV, respectively [45]. The CaO and SiO_2 nanoparticles are effectively functionalized on the collagen and silk fibroin nanofiber matrix to generate the composite nanofiber, according to the XPS spectrum of the COL/SF/CaO-SiO_2 composite.

3.6. Thermal analysis: thermogravimetric analysis (TGA) and differential scanning calorimetry (DSC) analysis

The thermal stability of composite nanofiber was analyzed by thermogravimetric (TGA) and differential scanning calorimetry (DSC) analysis. TGA was utilized to determine the composite nanofiber's thermal stability as well as its composition and purity. Each nanofiber material was put in an alumina crucible and heated at a rate of 10 °C/min between 20 and 800 °C in a nitrogen environment. The TGA curve of the COL nanofiber (Fig. 7 a.i) demonstrates that the nanofiber loses weight at five different temperatures: 125, 235, 352, 487, and 560 °C. The first weight loss at 125 °C corresponds to the removal of water molecules, whereas the second, third, fourth, and fifth weight losses at 235,352, 487, and 560 correspond to gelatin decomposition due to polypeptide bond breaking in amino acids [46,47]. The residual percentage of COL nanofiber after decomposition is −7.62%. There are no samples available up to 800 °C because of the low thermal stability of COL nanofiber. The TGA cure of COL/SF composite nanofiber (Fig. 7 a.ii.) exhibits weight loss at 120, 260, 375, 460, and 550 °C. The cause for the weight loss is virtually the same as the reason for the weight loss with COL nanofiber. The COL/SF nanofiber residual percentage is 4.242%. The rise in the residual percentage implies that the thermal stability of the nanofiber has improved. The addition of silk fibroin to collagen improves the thermal stability of the COL/SF composite nanofiber. Furthermore, the residual percentage was raised from −7.62 percent to 4.242%. Thermal stability improves, which is beneficial for biological applications. Furthermore, COL/SF/CaO-SiO_2 composite nanofiber (Fig. 7 a.iii) loses weight at 131, 248,

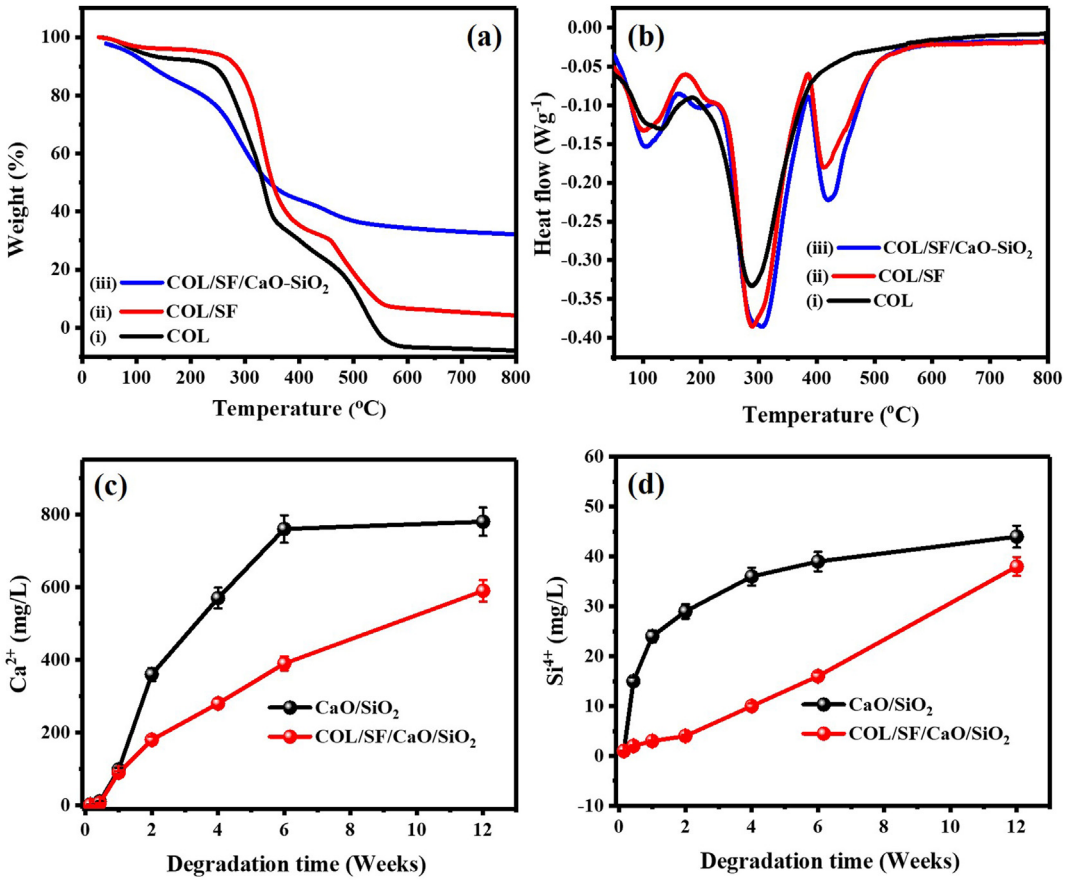

Fig. 7. (a) TGA, (b) DSC thermogram of COL (i), COL/SF (ii) and COL/SF/CaO-SiO_2 (iii) composite nanofiber. In-vitro degradation: The ion concentration of Ca^{2+} (c) and Si^{4+} (d) of CaO-SiO_2 and COL/SF/CaO-SiO_2 immersed in SBF solution.

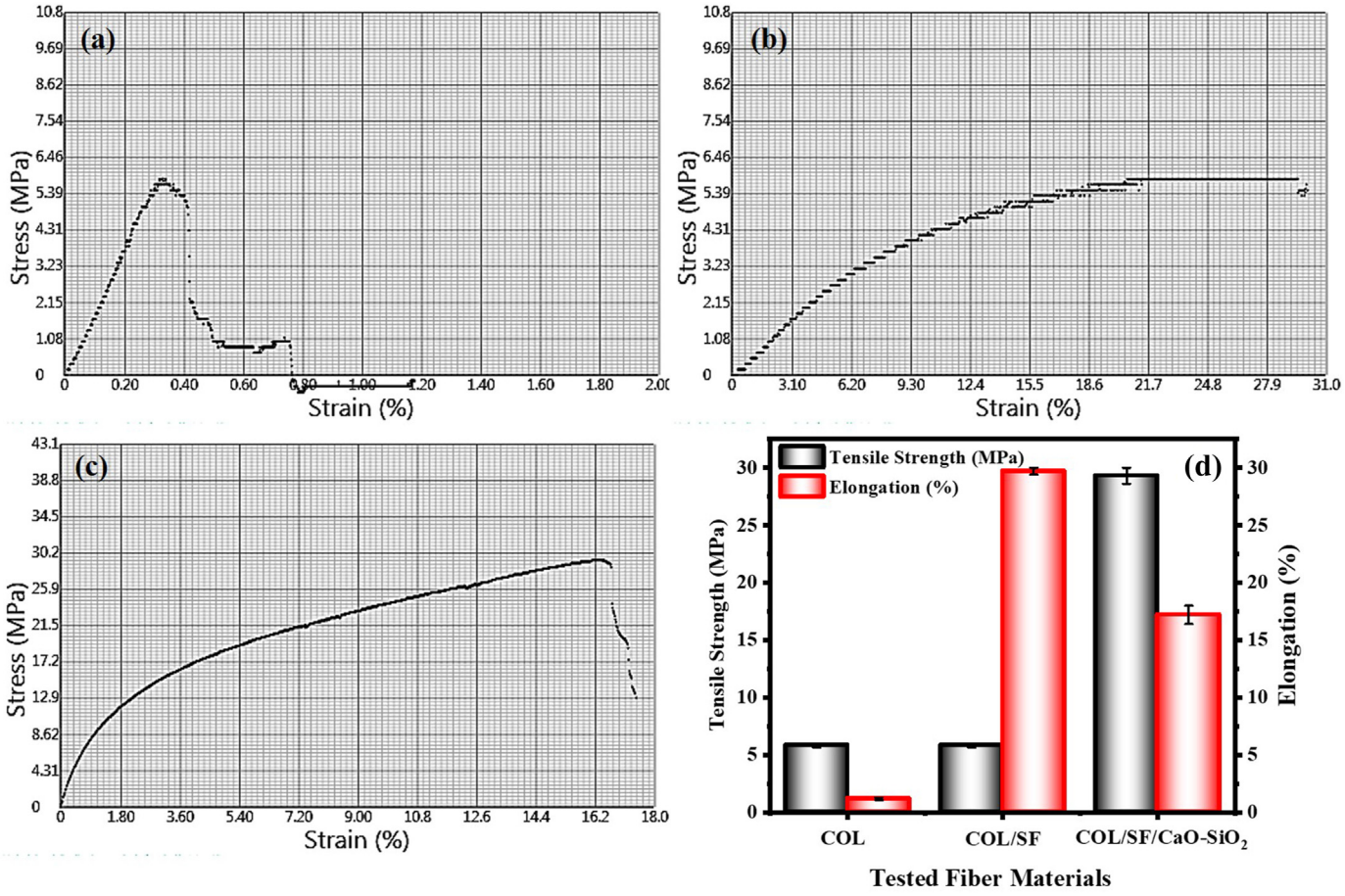

Fig. 8. Mechanical strength analysis of (a) COL (b) COL/SF (c) COL/SF/CaO-SiO_2 composite nanofiber and (d) Bar-diagram representation of the mechanical strength results of COL, COL/SF, COL/SF/CaO-SiO2 composite nanofiber.

Table 2
Mechanical properties of COL, COL/SF and COL/SF/CaO-SiO_2 composite nanofiber.

Samples	Tensile Strength (MPa)	Elongation (%)
COL	5.83 ± 0.17	1.08 ± 0.12
COL/SF	5.83 ± 0.17	29.70 ± 0.3
COL/SF/CaO-SiO2	29.30 ± 0.7	17.2 ± 0.8

377, 438, and 507 °C. The achieved weight loss peaks were almost equal to the COL and COL/SF nanofibrous matrix. Weight loss is produced by the breaking of peptide links in amino acids, which results in the disintegration of COL and SF [48]. Furthermore, bioactive glass (CaO/SiO_2) nanoparticles have thermal stability up to 800 °C, hence there is no weight loss related to bioactive glass nanoparticles. The residual percentage of COL/SF/CaO-SiO_2 composite nanofiber is 32.68%. The rise in residual percentage indicates the incorporation of nanoparticles into the nanofiber matrix. The addition of bioactive glass nanoparticles improves the thermal stability of composite nanofiber over pure material.

Furthermore, the thermodynamic characteristics of COL, COL/SF, and COL/SF/CaO-SiO_2 composite nanofibers were investigated using the differential scanning calorimetry (DSC) technique. Fig. 7 b shows the DSC curves of COL, COL/SF, and COL/SF/CaO-SiO_2 composite nanofibers recorded in nitrogen from room temperature to 800 °C. The DSC curves of all samples reveal a distinctive endothermic peak at about 80–150 °C related to the loss of adsorbed water. The DSC curve of COL exhibits (Fig. 7 b.i) endothermic peaks at 288 °C, which are attributable to the thermal degradation of the collagen polymer chain [49]. The thermogram of COL/SF nanofiber (Fig. 7 b.ii) exhibits transition temperatures of 290.54 °C and 413.37 °C, which are attributed to the decomposition of collagen and silk fibroin in the COL/SF nanofiber. In this thermogram, the denaturation temperature of SF was raised from 288 °C to 290.54 °C owing to the substantial cross-linking of collagen with silk fibroin [50]. The thermogram of COL/SF/CaO-SiO_2 (Fig. 7 b.iii) exhibits two distinct endothermic peaks at 308.54 °C and 419.87 °C, similar to COL/SF nanofiber, owing to the thermal degradation of collagen and silk fibroin polymer matrix [51]. The interaction of bioactive glass nanoparticles (CaO-SiO_2) with the polymer matrix raised the denaturation temperature of COL and SF. The addition of SF to the COL polymer matrix improves the composite fiber matrix's thermal characteristics. Furthermore, the intercalating behavior of CaO-SiO_2 nanoparticles improves the composite fiber's thermal stability. Interestingly, in an aqueous medium, this composite film does not easily flocculate.

3.7. In-vitro degradation analysis

To better comprehend the difference in degradation of CaO-SiO_2 and COL/SF/CaO-SiO_2 in in-vitro, Fig. 7 c&d depicted ionic concentration curves of Ca^{2+} and Si^{4+} with varied soaking times. According to the Ca^{2+} and Si^{4+}release curve, CaO-SiO_2 degraded quicker before 6 weeks, while COL/SF/CaO-SiO_2 degraded at a reasonably steady rate throughout the degradation period. The findings show that coating a layer of COL/SF on the surface of CaO-

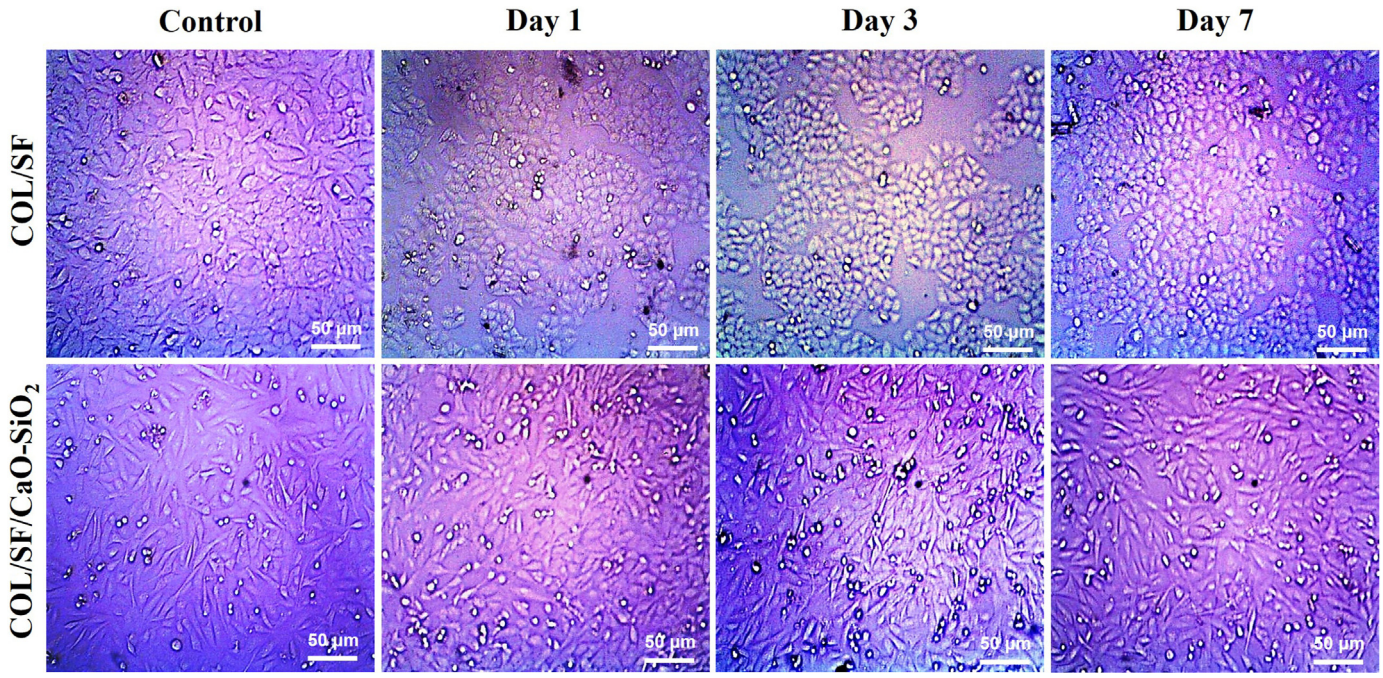

Fig. 9. In-vitro biocompatibility: Light microscopic images of Saos-2 osteo cells culture on COL/SF and COL/SF/CaO-SiO_2 scaffold for 1, 3 and 7 days.

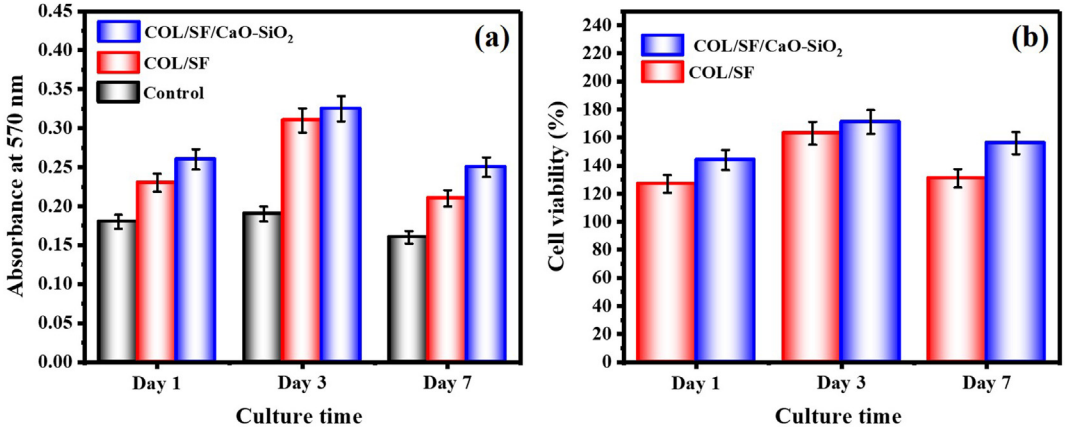

Fig. 10. In vitro biocompatibility: (a) MTT assay analysis and (b) biocompatibility of Saos-2 cell culture on COL/SF and COL/SF/CaO-SiO_2 scaffold after 1, 3 and 7 days.

SiO_2 may greatly extend the degradation rate of CaO-SiO_2 while also improving Ca^{2+} and Si^{4+} utilization. Based on the results of those studies, we can see that after 12 weeks of degradation, the majority of the CaO-SiO_2 scaffolds had been degraded, with just a little quantity of particles remaining in the degradation solution. The scaffold for COL/SF/CaO-SiO_2 has become loose, however, certain COL/SF/CaO-SiO_2 fibers have not entirely deteriorated.

3.8. Mechanical strength analysis

In the field of bone tissue engineering, mechanical performance is very important. Because of their outstanding biocompatibility, biodegradability, and ability to imitate the bone environment, collagen and silk fibroin were utilized as the binder materials for the fabrication of bioactive glass nanoparticles inserted COL/SF composite nanofiber. It was predicted that the incorporation of nanoparticles into the fibrous skeleton would aid in the enhancement of the mechanical characteristics of the nanofiber. The strength of a nanofiber is often determined by the biopolymer chemical bond interaction inside the polymer matrix as well as the interaction of nanoparticles. Fig. 8 shows the mechanical strength of fabricated collagen (COL), collagen/silk fibroin (COL/SF), and COL/SF/CaO-SiO_2 composite fiber. According to this finding, COL/SF/CaO-SiO_2 composite fiber has higher mechanical strength than other nanofibers. The mechanical strength of the composite fiber is improved by the incorporation of bioactive glass (CaO-SiO_2) nanoparticles into the polymer matrix. As predicted, the COL nanofiber (Fig. 8a) exhibits lower mechanical characteristics, with lesser TS (5.83 ± 0.17 MPa) and E % (1.08 ± 0.12) values. The COL/SF nanofiber's E % increased to 29.70 ± 0.3 MPa with the addition of silk fibroin to the collagen polymer matrix, while its TS value remained unchanged (Fig. 8b). The E % of COL/SF was raised because silk fibroin potentially serves as a plasticizer to enhance the flexibility of the composite films owing to the electrostatic interaction of two oppositely charged Polysaccharides [52,53]. The incorporation of bioactive glass (CaO-SiO_2) nanoparticles into the COL/SF

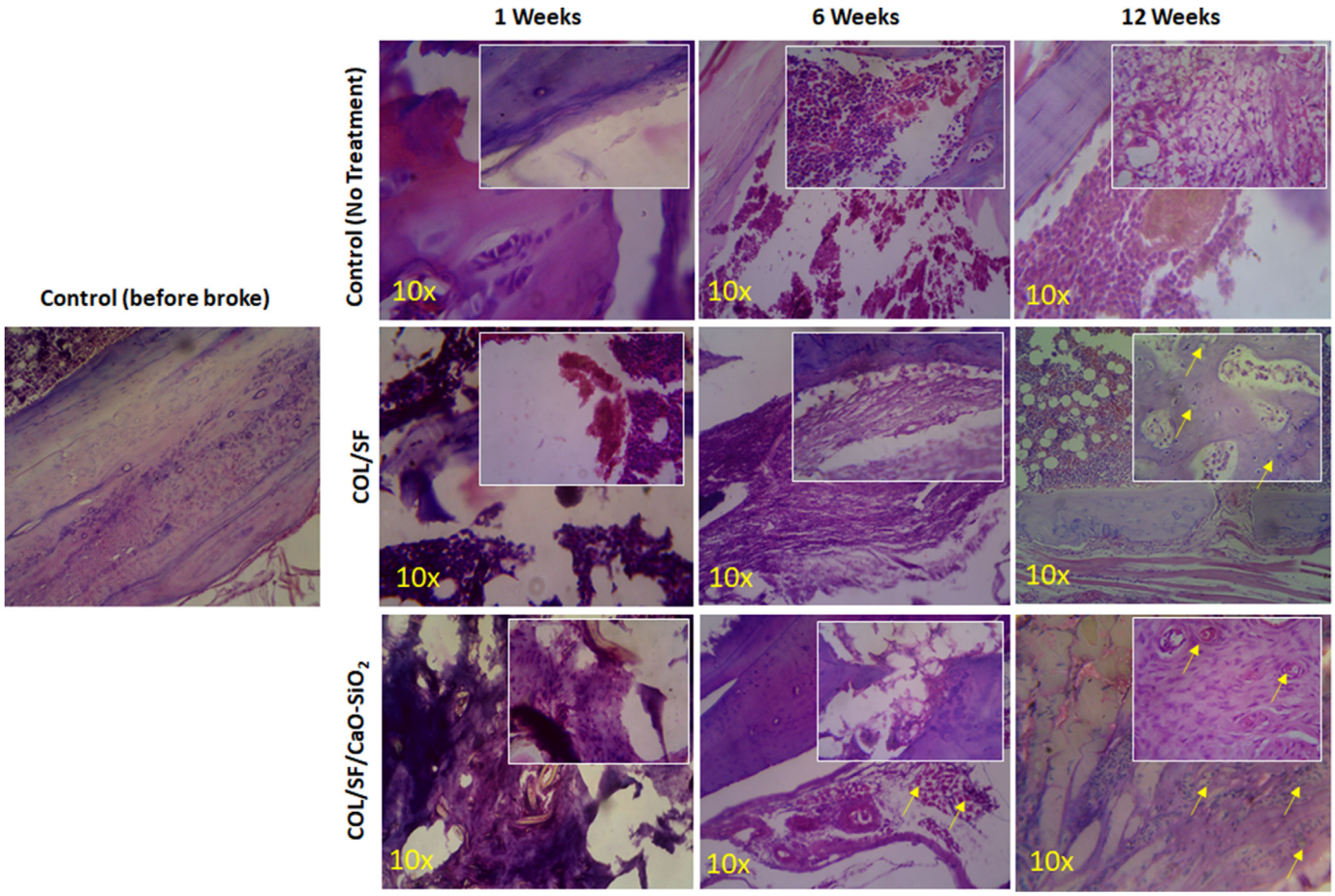

Fig. 11. H&E staining of osteoporotic bone defects in COL/SF group and COL/SF/CaO-SiO_2 group at 6 and 12 weeks after treatment.

fiber matrix fills the pores in the COL/SF fiber (Fig. 8c), increasing tensile strength (29.30 ± 0.7 MPa) while decreasing elongation % (17.2 ± 0.8%). According to the parameter (Table 2 & Fig. 8d), the COL/SF/CaO-SiO_2 composite nanofiber has low ductility and is more brittle. Those findings suggest that it is a biodegradable material when compared to other fiber materials and that its mechanical behavior is suited for clinical applications.

3.9. *In vitro biocompatibility and cell adhesion on the scaffold*

Osteoporotic bones have a limited ability to regenerate, making current therapies ineffective in achieving desired therapeutic outcomes. As a model system, osteosarcoma cell lines such as the Saos-2 cell line have been more popular in recent years. Osteoblastic development is possible with these cell lines because they can respond to chemical stimuli that promote osteoblastic differentiation and mimic the activity of mesenchymal stem cells (MSCs) in the early stages of cell attachment to biomaterials [54]. Bioactivity and biocompatibility of COL/SF and COL/SF-CaO-SiO_2 nanofiber scaffolds were initially evaluated in vitro using the MTT cell proliferation test on Saos-2 cells (Fig. 9). The remarkable bioactivity of COL/SF/CaO-SiO_2 nanofiber scaffolds was shown after just 7 days of cell culture by the deposition of superior minerals like calcium and silicon on COL/SF nanofibers in COL/SF/CaO-SiO_2 scaffolds compared to COL/SF nanofiber scaffolds. The biocompatibility of COL/SF and COL/SF/CaO-SiO_2 scaffold materials is superior to that of the blank control group (Fig. 10a). It was found that after 3 days, the optical density values of both the COL/SF scaffold and the COL/SF/CaO-SiO_2 scaffold were 0.325 and 0.31, respectively. This shows that both scaffolds had almost identical levels of biological compatibility. The apparent rise in the optical value on the 3rd day indicated that cells were able to thrive and multiply in the leaching solution of stents. There was a minor decline in optical density value on the 7th day, which may have been due to cell proliferation filling the orifice plate, leaving no more room for cells to multiply, as well as nutritional inadequacies.

Furthermore, based on the OD (optimal density) values of the relevant cultures, the cell viability (%) values of CA/SF and COL/SF/CaO-SiO_2 were calculated (Fig. 10b). On the first day of the experiment, the cell viability of the CA/SF and COL/SF/CaO-SiO_2 scaffolds was 127% and 144%, respectively. After three days in culture, the cell viability of the CA/SF and COL/SF/CaO-SiO_2 scaffolds had increased to 163 and 171%, respectively. The cell viability values of the CA/SF and COL/SF/CaO-SiO_2 scaffolds were reduced to 131 and 156%, respectively, due to the existence of a nutrient lake and inadequate area for cell development. These findings suggest that the COL/SF/CaO-SiO_2 composite nanofibers are extremely biocompatible, as shown by the high degree of osteosarcoma Saos-2 cell growth and viability.

Once osteoblast cells were grown on the scaffolds, SEM images were taken. Incredibly, 7 days after incubation, osteoblast cells (Figure SI1) had fully spread throughout the nanofiber's surface, with the cells' filopodia clearly visible in the SEM micrographs. These composite scaffolds show that the cells can be connected to the scaffold, and the cells can expand, suggesting that created biomimetic scaffolds might offer a good environment for the

development of osteoblast cells. Nanofiber-based composite scaffolds reinforced by ceramic nanoparticles are one of the unique strategies that have not been extensively researched until now, according to a review of the research in this area. Bioactive glasses and other silicate-based ceramics have also replaced calcium phosphate phases like Hydroxyapatite [55,56]. Bioactive glasses provide the opportunity to explore the possible impacts of various materials in biological habitats because of the variety of elements that may be included in their structure. The objective of this work was to employ a composite nanofiber scaffold based on collagen, silk fibroin, and bioactive CaO-SiO_2 nanoparticles because of the lack of research into the impact of these materials on bone tissue engineering. CaO-SiO_2 nanoparticles were generated using the given approach, and they were combined with COL/SF nanofibers to create a durable bone tissue engineering scaffold with an appropriate structure, as shown by the findings of this study. Furthermore, this study shows that COL/SF/CaO-SiO_2 composite nanofibers have the potential to be used as implants in bone tissue engineering applications.

3.10. Histological analysis of bone regeneration

Histological study revealed new bone growth in the osteoporotic defect region of rats treated with COL/SF and COL/SF/CaO-SiO_2. Six weeks following surgery, H&E staining (Fig. 11) revealed that new bone trabeculae had developed into the defect area's edge (the red region represents defect edge), and an abundance of osteoblasts had been seen in new bone and non-degradable materials (the blue dot represents osteo cell nucleus). Twelve weeks after implantation, in the COL/SF and COL/SF/CaO-SiO_2 groups, lamellar bone trabeculae formed near the defect's margin. Although COL/SF degraded more rapidly than COL/SF/CaO-SiO_2, the thickness and number of bone trabeculae were significantly reduced, and the trabeculae were densely packed with disordered fibrous and connective tissues, whereas COL/SF/CaO-SiO_2 produced more new bone and had no disordered fibrous tissue [57].

A further discovery of the MTS staining was the presence of more chondrocytes and cartilage transitioning to the bone in the COL/SF and COL/SF/CaO-SiO_2 groups (Fig. 12) after 6 weeks after surgery (shown in the image as the red-banded area). The maturity of new bone in the defect location of the COL/SF and COL/SF/CaO-SiO_2 groups increased with increasing implantation time (bright green). In contrast to the COL/SF group, the COL/SF/CaO-SiO_2 group's defect area showed more bright green trabeculae and the trabeculae were distributed more evenly and compactly with smaller spacing, indicating that the cartilage transforming into mature bone had not yet occurred in the COL/SF group's defect area [58]. With a longer degradation time, it is feasible that COL/SF/CaO-SiO_2 can keep up with the rate of new bone growth and have greater bone regeneration capacities.

Immunohistochemical analysis was used to investigate the expression of osteogenesis, angiogenesis, and bone metabolism markers in the tibial defect region of OVX rats in the COL/SF and COL/SF/CaO-SiO_2 groups (Fig. 13). At 12 weeks after surgery, both the COL/SF and COL/SF/CaO-SiO_2 groups expressed CD31 and OCN in the bone defect area; however, the expression of angiogenesis and osteogenic markers was higher in the COL/SF/CaO-SiO_2 group, indicating that the COL/SF/CaO-SiO_2 group may be able to promote new blood vessel and bone formation (as shown by the red circle in the Fig. 13) [59,60]. Using the OPG antibody to measure bone-metabolism indicators, the COL/SF group suppressed osteoclast

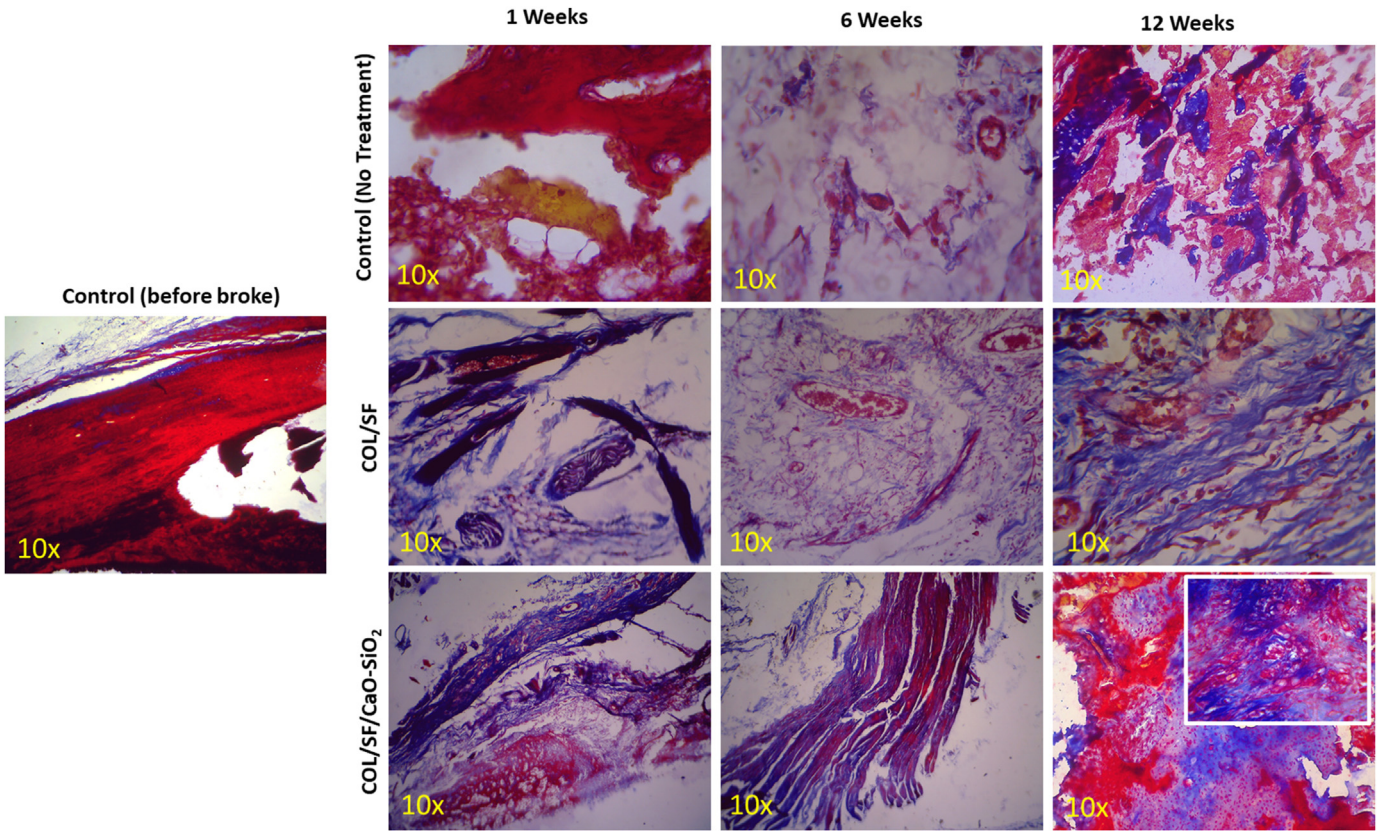

Fig. 12. Masson-Goldner stained osteoporotic bone defects in COL/SF group and COL/SF/CaO-SiO_2 group at 6 and 12 weeks after treatment.

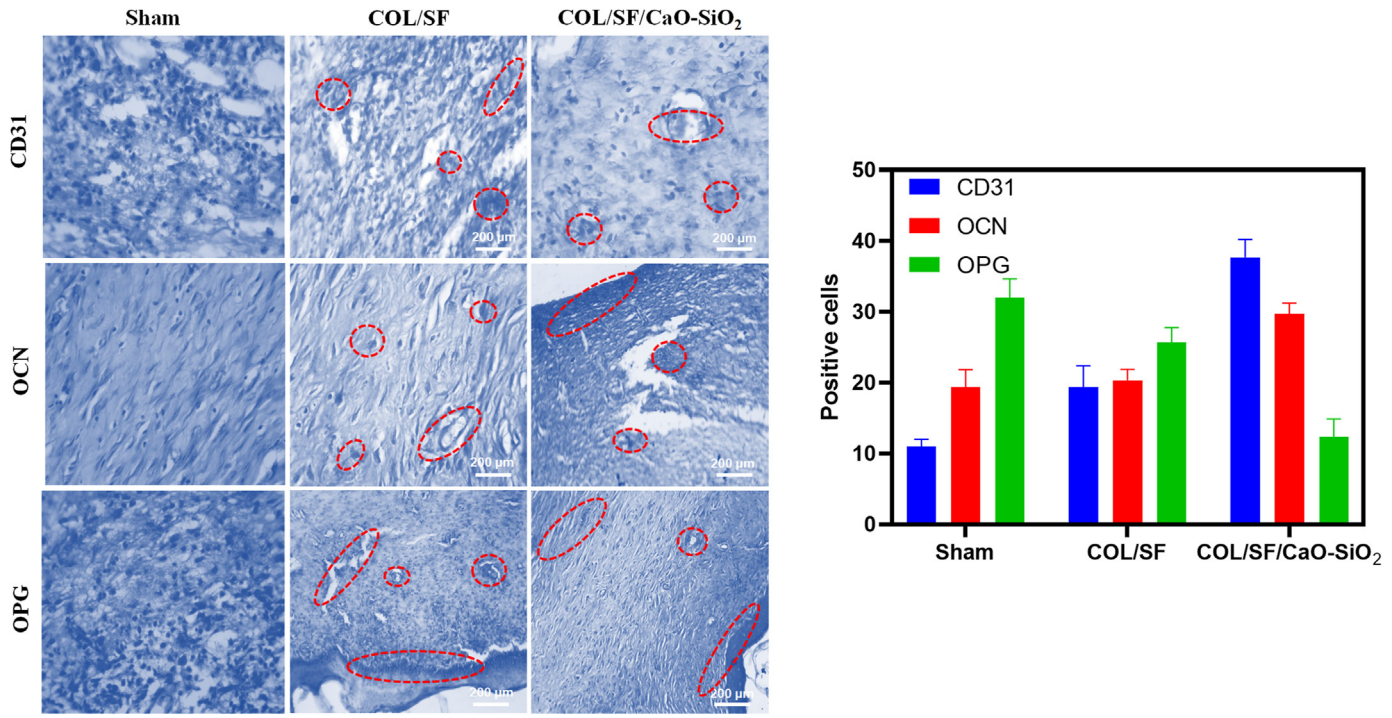

Fig. 13. Immunohistochemical investigation of CD31, OCN OPG and after 12 weeks treatment in OVX bone defects.

activity in the bone defect region by a wider margin than the COL/SF group by week 12. According to the results, COL/SF/CaO-SiO_2 implantation improved angiogenesis and bone development while also boosting bone metabolism.

4. Conclusion

In conclusion, the electrospinning technique was used to successfully fabricate the COL/SF/CaO-SiO_2 composite nanofiber. The bioactive glass (CaO-SiO2) nanoparticles were prepared using the sol-gel process when coupled with a blended solution of collagen (COL) and silk fibroin (SF), and the composite solution was electrospun. The lone pair of electrons at the nitrogen site of amino groups in COL and SF coupled with bioactive glass (CaO-SiO_2) nanoparticles during electrospinning, resulted in the production of CaO-SiO_2 nanoparticles on the surfaces of the COL/SF fiber matrix. The XRD spectrum revealed that the 37 nm grain-sized crystalline CaO-SiO_2 nanoparticles were attached to the COL/SF composite fiber matrix. Further. The FTIR spectrum further supports the presence of amino acids, carbonyl functional groups, Ca-O, and Si-O functionalities in the composite fiber matrix. The fabricated nanofiber has a needle and sticks shape morphology with an average diameter size of 105.63 ± 10 nm as determined by SEM examination, and the associated EDX spectrum and mapping demonstrate the existence and uniform distribution of C, N, O, Ca, and Si elements in the composite nanofiber. The HR-TEM examination validated the formation of needle-shaped fibers with an average diameter of 115 ± 10 nm in the COL/SF/CaO-SiO_2 composite nanofiber, and it also selectively revealed bioactive glass nanoparticles such as CaO-SiO_2 with an average size of 20 ± 5 nm. The peaks in the XPS spectra at 284eV, 398eV, 531eV, 347eV, and 104eV revealed the existence of C, N, O, Ca, and Si in the composite fiber matrix. Furthermore, the high-resolution spectrum demonstrates how COL and SF combine to form the COL/SF fiber matrix, as well as how CaO-SiO_2 nanoparticles interact with the COL/SF fiber matrix. TGA investigation indicated that the COL/SF/CaO-SiO_2 composite nanofiber had the highest thermal stability, with a residual percentage of 32.68%. Bioactive glass nanoparticle doping enhances the thermal stability of nanofibers. This thermal stability is beneficial in the treatment of osteoporotic bone. According to in-vitro degradation experiments, CaO-SiO2 decomposed faster before 6 weeks, while COL/SF/CaO-SiO_2 degraded at a pretty consistent pace throughout the degradation period. Furthermore, The MTT cell proliferation assay on Saos-2 cells was also used to evaluate nanofiber biocompatibility. According to the findings, COL/SF/CaO-SiO_2 composite nanofiber has no negative impact on Saos-2 cell proliferation. The COL/SF/CaO-SiO_2 cement with a longer degradation time matched the pace of bone formation and demonstrated improved bone growth performance in the OVX rats' in vivo critical-sized bone defect, as validated by histological examination. Additionally, data from immunohistochemistry demonstrated that COL/SF/CaO-SiO_2 may produce a Ca^{2+} and Si^{4+} rich ambiance for the defect region, increase blood vessel development, mineral deposition, and improve bone metabolism. It is envisaged that COL/SF/CaO-SiO_2 based bone cement would be employed to repair osteoporotic bone defects because of its outstanding osteogenic activity and regulated degradation in localized areas in both laboratory and animal tests.

Declaration of competing interest

We declare that we have no financial and personal relationships with other people or organizations that can inappropriately influence our work, there is no professional or other personal interest of any nature or kind in any product, service and/or company that could be construed as influencing the position presented in, or the review of, the manuscript entitled "**Fabrication of Biologically Inspired Electrospun Collagen/Silk fibroin/Bioactive glass composited Nanofibrous scaffold to accelerate the Treatment efficiency of Bone repair**".

Acknowledgment

This research is financially supported by Fujian Natural Science Foundation Project (2018J01364), PR China.

Appendix A. Supplementary data

Supplementary data to this article can be found online at https://doi.org/10.1016/j.reth.2022.05.006.

References

[1] Fuggle NR, Curtis EM, Ward KA, Harvey NC, Dennison EM, Cooper C. Fracture prediction, imaging and screening in osteoporosis. Nat Rev Endocrinol 2019 Sep;15(9):535–47.
[2] Zhao H, Li X, Zhang D, Chen H, Chao Y, Wu K, et al. Integrative bone metabolomics—lipidomics strategy for pathological mechanism of postmenopausal osteoporosis mouse model. Sci Rep 2018 Nov 7;8(1). 1-1.
[3] Liang C, Peng S, Li J, Lu J, Guan D, Jiang F, et al. Inhibition of osteoblastic Smurf1 promotes bone formation in mouse models of distinctive age-related osteoporosis. Nat Commun 2018 Aug 24;9(1):1–4.
[4] Mora-Raimundo P, Lozano D, Manzano M, Vallet-Regí M. Nanoparticles to knockdown osteoporosis-related gene and promote osteogenic marker expression for osteoporosis treatment. ACS Nano 2019 May 9;13(5):5451–64.
[5] Zhang Y, Wei L, Miron RJ, Shi B, Bian Z. Bone scaffolds loaded with siRNA-Semaphorin4d for the treatment of osteoporosis related bone defects. Sci Rep 2016 Jun 2;6(1):1–9.
[6] Weng L, Boda SK, Teusink MJ, Shuler FD, Li X, Xie J. Binary doping of strontium and copper enhancing osteogenesis and angiogenesis of bioactive glass nanofibers while suppressing osteoclast activity. ACS Appl Mater Interfaces 2017 Jul 26;9(29):24484–96.
[7] Weng L, Boda SK, Wang H, Teusink MJ, Shuler FD, Xie J. Novel 3D hybrid nanofiber aerogels coupled with BMP-2 peptides for cranial bone regeneration. Adv Healthcare materials 2018 May;7(10):1701415.
[8] Ding Y, Xu W, Wang W, Fong H, Zhu Z. Scalable and facile preparation of highly stretchable electrospun PEDOT: PSS@ PU fibrous nonwovens toward wearable conductive textile applications. ACS Appl Mater Interfaces 2017 Sep 6;9(35):30014–23.
[9] Ratakonda S, Sridhar UM, Rhinehart RR, Madihally SV. Assessing viscoelastic properties of chitosan scaffolds and validation with cyclical tests. Acta Biomater 2012 Apr 1;8(4):1566–75.
[10] Correia CO, Mano JF. Chitosan scaffolds with a shape memory effect induced by hydration. J Mater Chem B 2014;2(21):3315–23.
[11] Ma J, Chen CZ, Wang DG, Meng XG, Shi JZ. Influence of the sintering temperature on the structural feature and bioactivity of sol–gel derived SiO2–CaO–P2O5 bioglass. Ceram Int 2010 Aug 1;36(6):1911–6.
[12] Micoulaut M, Yue Y. Material functionalities from molecular rigidity: maxwell's modern legacy. MRS Bull 2017 Jan;42(1):18–22.
[13] Mead RN, Mountjoy G. A molecular dynamics study of the atomic structure of (CaO) x (SiO2) 1-x Glasses. J Phys Chem B 2006 Jul 27;110(29):14273–8.
[14] Diba M, Camargo WA, Brindisi M, Farbod K, Klymov A, Schmidt S, et al. Composite colloidal gels made of bisphosphonate-functionalized gelatin and bioactive glass particles for regeneration of osteoporotic bone defects. Adv Funct Mater 2017 Dec;27(45):1703438.
[15] Behring J, Junker R, Walboomers XF, Chessnut B, Jansen JA. Toward guided tissue and bone regeneration: morphology, attachment, proliferation, and migration of cells cultured on collagen barrier membranes. A Systematic Rev Odontology 2008 Jul;96(1). 1-1.
[16] Heinemann S, Coradin T, Worch H, Wiesmann HP, Hanke T. Possibilities and limitations of preparing silica/collagen/hydroxyapatite composite xerogels as load-bearing biomaterials. Compos Sci Technol 2011 Nov 14;71(16):1873–80.
[17] Heinemann S, Heinemann C, Ehrlich H, Meyer M, Baltzer H, Worch H, et al. A novel biomimetic hybrid material made of silicified collagen: perspectives for bone replacement. Adv Eng Mater 2007 Dec;9(12):1061–8.
[18] Zhang Y, Huang J, Huang L, Liu Q, Shao H, Hu X, et al. Silk fibroin-based scaffolds with controlled delivery order of VEGF and BDNF for cavernous nerve regeneration. ACS Biomater Sci Eng 2016 Nov 14;2(11):2018–25.
[19] Zhang W, Zhu C, Ye D, Xu L, Zhang X, Wu Q, et al. Porous silk scaffolds for delivery of growth factors and stem cells to enhance bone regeneration. PLoS One 2014 Jul 22;9(7):e102371.
[20] Zhang YS, Khademhosseini A. Advances in engineering hydrogels. Science 2017 May 5;(6337):356.
[21] Cui H, Yu Y, Li X, Sun Z, Ruan J, Wu Z, et al. Direct 3D printing of a tough hydrogel incorporated with carbon nanotubes for bone regeneration. J Mater Chem B 2019;7(45):7207–17.
[22] Shi W, Sun M, Hu X, Ren B, Cheng J, Li C, et al. Structurally and functionally optimized silk-fibroin–gelatin scaffold using 3D printing to repair cartilage injury in vitro and in vivo. Adv Mater 2017 Aug;29(29):1701089.
[23] Shi L, Wang F, Zhu W, Xu Z, Fuchs S, Hilborn J, et al. Self-healing silk fibroin-based hydrogel for bone regeneration: dynamic metal-ligand self-assembly approach. Adv Funct Mater 2017 Oct;27(37):1700591.
[24] Gao F, Xu Z, Liang Q, Liu B, Li H, Wu Y, et al. Direct 3D printing of high strength biohybrid gradient hydrogel scaffolds for efficient repair of osteochondral defect. Adv Funct Mater 2018 Mar;28(13):1706644.
[25] Wang L, Qiu Y, Lv H, Si Y, Liu L, Zhang Q, et al. 3D Superelastic scaffolds constructed from flexible inorganic nanofibers with self-fitting capability and tailorable gradient for bone regeneration. Adv Funct Mater 2019 Aug;29(31):1901407.
[26] Kamata H, Akagi Y, Kayasuga-Kariya Y, Chung UI, Sakai T. Nonswellable" hydrogel without mechanical hysteresis. Science 2014 Feb 21;343(6173):873–5.
[27] Lei Z, Wang Q, Sun S, Zhu W, Wu P. A bioinspired mineral hydrogel as a self-healable, mechanically adaptable ionic skin for highly sensitive pressure sensing. Adv Mater 2017 Jun;29(22):1700321.
[28] Mohan N, Wilson J, Joseph D, Vaikkath D, Nair PD. Biomimetic fiber assembled gradient hydrogel to engineer glycosaminoglycan enriched and mineralized cartilage: an in vitro study. J Biomed Mater Res 2015 Dec;103(12):3896–906.
[29] Phillips DM, Drummy LF, Conrady DG, Fox DM, Naik RR, Stone MO, et al. Dissolution and regeneration of Bombyx mori silk fibroin using ionic liquids. J Am Chem Soc 2004 Nov 10;126(44):14350–1.
[30] Huang Q, Li X, Liu T, Wu H, Liu X, Feng Q, et al. Enhanced SaOS-2 cell adhesion, proliferation and differentiation on Mg-incorporated micro/nano-topographical TiO2 coatings. Appl Surf Sci 2018 Jul 31;447:767–76.
[31] Lee EJ, Shin DS, Kim HE, Kim HW, Koh YH, Jang JH. Membrane of hybrid chitosan–silica xerogel for guided bone regeneration. Biomaterials 2009 Feb 1;30(5):743–50.
[32] Sun TW, Zhu YJ, Chen F, Zhang YG. Ultralong hydroxyapatite nanowire/collagen biopaper with high flexibility, improved mechanical properties and excellent cellular attachment. Chem–An Asian J 2017 Mar 16;12(6):655–64.
[33] Li M, Lu S, Wu Z, Tan K, Minoura N, Kuga S. Structure and properties of silk fibroin–poly (vinyl alcohol) gel. Int J Biol Macromol 2002 Apr 8;30(2):89–94.
[34] Su H, Han J, Dong Q, Xu J, Chen Y, Gu Y, et al. In situ bioinspired synthesis of silver chloride nanocrystals on silk fibroin fibers. Appl Phys A 2011 Feb;102(2):429–34.
[35] Wang L, Qiu Y, Guo Y, Si Y, Liu L, Cao J, et al. Smart, elastic, and nanofiber-based 3D scaffolds with self-deploying capability for osteoporotic bone regeneration. Nano Lett 2019 Nov 25;19(12):9112–20.
[36] Riaz T, Zeeshan R, Zarif F, Ilyas K, Muhammad N, Safi SZ, et al. FTIR analysis of natural and synthetic collagen. Appl Spectrosc Rev 2018 Oct 21;53(9):703–46.
[37] Dhinasekaran D, Selvaraj V, Rajendran AR, Saravanan S, Purushothaman B, Subramaniam B. Bio-inspired multifunctional collagen/electrospun bioactive glass membranes for bone tissue engineering applications. Mater Sci Eng C 2021 Jan 6:111856.
[38] Yang Z, Peng H, Wang W, Liu T. Crystallization behavior of poly (ε-caprolactone)/layered double hydroxide nanocomposites. J Appl Polym Sci 2010 Jun 5;116(5):2658–67.
[39] Kikuchi M, Itoh S, Ichinose S, Shinomiya K, Tanaka J. Self-organization mechanism in a bone-like hydroxyapatite/collagen nanocomposite synthesized in vitro and its biological reaction in vivo. Biomaterials 2001 Jul 1;22(13):1705–11.
[40] Chang MC, Tanaka J. FT-IR study for hydroxyapatite/collagen nanocomposite cross-linked by glutaraldehyde. Biomaterials 2002 Dec 1;23(24):4811–8.
[41] Almasian A, Fard GC, Mirjalili M, Gashti MP. Fluorinated-PAN nanofibers: preparation, optimization, characterization and fog harvesting property. J Ind Eng Chem 2018 Jun 25;62:146–55.
[42] Hildebrandt M, Shin EY, Yang S, Ali W, Altinpinar S, Gutmann JS. Investigation of roughness correlation in polymer brushes via X-ray scattering. Polymers 2020 Sep;12(9):2101.
[43] Chandran P, Ghosh A, Ramaprabhu S. High-performance Platinum-free oxygen reduction reaction and hydrogen oxidation reaction catalyst in polymer electrolyte membrane fuel cell. Sci Rep 2018 Feb 26;8(1). 1-1.
[44] Rao RG, Blume R, Hansen TW, Fuentes E, Dreyer K, Moldovan S, et al. Interfacial charge distributions in carbon-supported palladium catalysts. Nat Commun 2017 Aug 24;8(1). 1-0.
[45] El-Fiqi A, Kim HW. Sol-gel synthesis and characterization of novel cobalt ions-containing mesoporous bioactive glass nanospheres as hypoxia and ferroptosis-inducing nanotherapeutics. J Non-Cryst Solids 2021 Oct 1;569:120999.
[46] Mitropoulos AN, Burpo FJ, Nguyen CK, Nagelli EA, Ryu MY, Wang J, et al. Noble metal composite porous silk fibroin aerogel fibers. Materials 2019 Jan;12(6):894.
[47] Liu Y, Deng L, Zhang C, Feng F, Zhang H. Tunable physical properties of ethylcellulose/gelatin composite nanofibers by electrospinning. J Agric Food Chem 2018 Feb 28;66(8):1907–15.
[48] Venugopal K, Ahmad H, Manikandan E, Arul KT, Kavitha K, Moodley MK, et al. The impact of anticancer activity upon Beta vulgaris extract mediated biosynthesized silver nanoparticles (ag-NPs) against human breast (MCF-7), lung (A549) and pharynx (Hep-2) cancer cell lines. J Photochem Photobiol B Biol 2017 Aug 1;173:99–107.
[49] Gauza-Włodarczyk M, Kubisz L, Mielcarek S, Włodarczyk D. Comparison of thermal properties of fish collagen and bovine collagen in the temperature range 298–670 K. Mater Sci Eng C 2017 Nov 1;80:468–71.
[50] An B, DesRochers TM, Qin G, Xia X, Thiagarajan G, Brodsky B, et al. The influence of specific binding of collagen–silk chimeras to silk biomaterials on hMSC behavior. Biomaterials 2013 Jan 1;34(2):402–12.

[51] Romero-Sánchez LB, Borrego-González S, Díaz-Cuenca A. High surface area biopolymeric-ceramic scaffolds for hard tissue engineering. Biomed Phys Eng Express 2017 May 11;3(3):035012.
[52] Burleigh MC, Brigfs AD, Lendon CL, Davies MJ, Born GV, Richardson PD. Collagen types I and III, collagen content, GAGs and mechanical strength of human atherosclerotic plaque caps: span-wise variations. Atherosclerosis 1992 Sep 1;96(1):71–81.
[53] Jiang S, Yu Z, Zhang L, Wang G, Dai X, Lian X, et al. Effects of different aperture-sized type I collagen/silk fibroin scaffolds on the proliferation and differentiation of human dental pulp cells. Regenerative Biomater 2021 Aug;8(4):rbab028.
[54] Tabb MM, Sun A, Zhou C, Grün F, Errandi J, Romero K, et al. Vitamin K2 regulation of bone homeostasis is mediated by the steroid and xenobiotic receptor SXR. J Biol Chem 2003 Nov 7;278(45):43919–27.
[55] Azami M, Tavakol S, Samadikuchaksaraei A, Hashjin MS, Baheiraei N, Kamali M, et al. A porous hydroxyapatite/gelatin nanocomposite scaffold for bone tissue repair: in vitro and in vivo evaluation. J Biomater Sci Polym Ed 2012 Dec 1;23(18):2353–68.
[56] Farokhi M, Mottaghitalab F, Shokrgozar MA, Ai J, Hadjati J, Azami M. Bio-hybrid silk fibroin/calcium phosphate/PLGA nanocomposite scaffold to control the delivery of vascular endothelial growth factor. Mater Sci Eng C 2014 Feb 1;35:401–10.
[57] Lin K, Xia L, Li H, Jiang X, Pan H, Xu Y, et al. Enhanced osteoporotic bone regeneration by strontium-substituted calcium silicate bioactive ceramics. Biomaterials 2013 Dec 1;34(38):10028–42.
[58] Zhang Y, Cheng N, Miron R, Shi B, Cheng X. Delivery of PDGF-B and BMP-7 by mesoporous bioglass/silk fibrin scaffolds for the repair of osteoporotic defects. Biomaterials 2012 Oct 1;33(28):6698–708.
[59] Niu CC, Tsai TT, Fu TS, Lai PL, Chen LH, Chen WJ. A comparison of posterolateral lumbar fusion comparing autograft, autogenous laminectomy bone with bone marrow aspirate, and calcium sulphate with bone marrow aspirate: a prospective randomized study. Spine 2009 Dec 1;34(25):2715–9.
[60] Subramaniam S, Fang YH, Sivasubramanian S, Lin FH, Lin CP. Hydroxyapatite-calcium sulfate-hyaluronic acid composite encapsulated with collagenase as bone substitute for alveolar bone regeneration. Biomaterials 2016 Jan 1;74:99–108.